2	Dublished ass
2	Published as:
3	Gao S, Hofstra AH, Zou X, Valley JW, Kitajima K, Marsh EE, Lowers HA, Adams DT, Qin K, Xu H (2021) Oxygen isotope evidence for input of magmatic fluids and precipitation of
5	Au-Ag-tellurides in an otherwise ordinary adularia-sericite epithermal system in NE
6	China. Am. Mineral., 106: 2003-2019. doi.org/10.2138/am-2021-7825
7	
8	Oxygen isotope evidence for input of magmatic fluids and precipitation of Au-Ag-
9	tellurides in an otherwise ordinary adularia-sericite epithermal system in NE China
10	Shen Gao ^{1, 2*} (<i>Corresponding Author</i>), Albert H. Hofstra ³ , Xinyu Zou ^{1, 2} , John W.
11	Valley ⁴ , Kouki Kitajima ⁴ , Erin E. Marsh ³ , Heather A. Lowers ³ , David T. Adams ³ ,
12	Kezhang Qin ^{1, 2, 5} , Hong Xu ⁶
13	¹ Key Laboratory of Mineral Resources, Institute of Geology and Geophysics, Chinese
14	Academy of Sciences, Beijing 100029, China
15	² Innovation Academy for Earth Science, Chinese Academy of Sciences, Beijing 100029,
16	China
17	³ U.S. Geological Survey, P.O. Box 25046, Denver, CO 80225, USA
18	⁴ WiscSIMS, Department of Geoscience, University of Wisconsin-Madison, 1215 West
19	Dayton Street, Madison, WI 53706, USA
20	⁵ University of Chinese Academy of Sciences, Beijing 100049, China
21	⁶ School of Earth Sciences and Resources, China University of Geosciences (Beijing),
22	Beijing 100083, China

Draft of Nov. 11, 2020

24

25

26

27

28

29

30

31

32

33

34

35

36

37

38

39

40

41

42

43

Tellurium (Te)-rich adularia-sericite epithermal Au-Ag deposits are an important current and future source of precious and critical metals. However, the source and evolution of ore-forming fluids in these deposits are masked by traditional bulk analysis of quartz oxygen isotope ratios that homogenize fine scale textures and growth zones. To advance understanding of the source of Te and precious metals, herein, we use petrographic and cathodoluminescence (CL) images of such textures and growth zones to guide high spatial resolution SIMS oxygen isotope analyses (10-µm spot) and spatially correlated fluid inclusion microthermometric measurements on successive quartz bands in contemporary Te-rich and Te-poor adularia-sericite (-quartz) epithermal Au-Ag vein deposits in northeastern China. The results show that large positive oxygen isotope shifts from -7.1 to +7.7% in quartz rims are followed by precipitation of Au-Ag telluride minerals in the Terich deposit, whereas small oxygen isotope shifts of only 4‰ (-2.2 to +1.6‰) were detected in quartz associated with Au-Ag minerals in the Te-poor deposits. Moreover, fluidinclusion homogenization temperatures are higher in comb quartz rims (avg. 266.4 to 277.5°C) followed by Au-Ag telluride minerals than in previous stages (~250°C) in the Terich deposit. The Te-poor deposit has a consistent temperature (~245°C) in quartz that preand post-dates Au-Ag minerals. Together, the coupled increase in oxygen isotope ratios and homogenization temperatures followed by precipitation of Au-Ag tellurides proves that inputs of magmatic fluid containing Au, Ag, and Te into barren meteoric water dominated flow systems are critical to formation of Te-rich adularia-sericite epithermal Au-Ag
deposits. In contrast, Te-poor adularia-sericite epithermal Au-Ag deposits show little or no
oxygen isotope or fluid inclusion evidence for inputs of magmatic fluid.

Key words: quartz, SIMS, oxygen isotopes, fluid inclusions, magmatic fluid, Te,
49 epithermal Au-Ag deposits

1. Introduction

Tellurium (Te)-rich adularia-sericite epithermal Au-Ag deposits are important producers of gold throughout the world (Ahmad et al. 1987; Spry et al. 1996; Cooke and McPhail 2001; Cook and Ciobanu 2005; Ciobanu et al. 2006; Voudouris 2006; Cook et al. 2009; Saunders and Brueseke 2012; Goldfarb et al. 2016, 2017; Kelley and Spry 2016; Zhai et al. 2018; Keith et al. 2020). Some of these deposits are associated with alkalic volcano-plutonic centers (e.g., Cripple Creek; Kelley et al. 1998) and others with calcalkalic volcano-plutonic centers (e.g., Sandaowanzi; Gao et al. 2017). Furthermore, the magmatic belts that contain Te-rich Au-Ag deposits can also host Te-poor Au-Ag deposits (e.g., Dong'an; Zhang et al. 2010a and reference therein). The source of Te in continental magmatic belts has been attributed to the nature of Sub Continental Lithospheric Mantle (SCLM) (e.g., Holwell et al. 2019). These deposits are economically important and are a potential source of Te, which is a critical commodity for modern technology, if current

65 metallurgical and economic impediments are resolved (Spry et al. 2004; Ciobanu et al.

2006; Cook et al. 2009; Goldfarb et al. 2016, 2017; Kelley and Spry 2016; Jenkin et al.

67 2019).

68

69

70

71

72

73

74

75

76

77

78

79

80

81

82

83

84

85

66

In magmatic-hydrothermal systems, Te is generally interpreted to be derived from igneous intrusions (Jensen and Barton 2000; Saunders and Brueseke 2012; Kelley and Spry 2016; Holwell et al. 2019), thus, magmatic fluids have been proposed to be involved in the formation of Te-rich epithermal Au-Ag deposits (e.g., Ciobanu et al. 2006). Recently, highprecision in-situ oxygen isotope analyses by ion microprobe are regarded to be the most effective way to detect short-lived oxygen isotope variations, which can record transient variations of fluid inputs in hydrothermal ore deposits (Valley and Graham, 1996; Smith et al. 1998; Valley et al., 1998; Saunders et al., 2008; Tanner et al., 2013; Fekete et al., 2016; Cernuschi et al., 2018; Li et al., 2019; Haroldson et al., 2020). However, in-situ isotopic evidence in Te-rich epithermal Au-Ag deposits is scarce, thus, the role of magmatic fluids in Te-rich epithermal Au-Ag deposits is still unclear. The large range of oxygen isotope values in quartz obtained by conventional technique from Te-rich epithermal deposits allows several interpretations. The highest $\delta^{18}O(Qz)$ values of up to 20% (e.g., Cripple Creek, Beaty 1996) are indicative of a magmatic fluid dominated system (e.g., Taylor 1997; Hedenquist et al. 1998). In contrast, many other deposits have lower δ^{18} O values close to 0‰, such as Tongyoung (Korea) ~3‰ (Shelton et al. 1990) and Sandaowanzi (northeast China) from -3.9 to -0.2% (Wu et al., 2005a; Zhai et al. 2018) that are indicative of meteoric water dominated systems (O'Neil and Silberman 1974; Hedenquist and Lowenstern 1994; Simmons 1995; Cooke and Simmons 2000; John et al. 2003; Simmons et al. 2005). The low oxygen isotope values raise the question: Is magmatic fluid needed to form a Te-rich Au-Ag deposit? If needed, what process causes Au-Ag telluride minerals to precipitate from magmatic fluids in epithermal systems? (e.g., fluid boiling, mixing of magmatic fluid with meteoric water, or cooling; Anderson and Eaton 1990; Cooke and McPhail 2001; Zhai et al. 2018). How do ore-forming processes differ between Te-rich and Te-poor epithermal Au-Ag deposits with low oxygen isotope values? (e.g., $\delta^{18}O=7-9\%$ at Hishikari, Japan; $\delta^{18}O=-3.0$ to 1.5% at Dong'an, northeastern China; Faure et al. 2002; Han 2013).

To investigate these questions, we studied the contemporary Te-rich Sandaowanzi and Te-poor Dong'an adularia-sericite epithermal Au-Ag deposits situated in an Early Cretaceous continental magmatic arc in northeastern China. We used mineral textures and cathodoluminescence (CL) imaging to guide high spatial resolution SIMS oxygen isotope analyses in combination with fluid inclusion microthermometric measurements of the same generation of quartz to advance understanding of the source and evolution of hydrothermal fluids in these two deposits. The results show that there is a large difference in the oxygen isotope ratios of quartz in associated with Te-rich vs. Te-poor Au-Ag mineralization in these deposits. In combination with fluid inclusion homogenization temperatures, the results reveal the evolution of hydrothermal fluids and mechanisms of mineral precipitation.

This study highlights the role of magmatic fluid inputs to formation of high-grade Au, Ag and Te veins and the importance of correlating oxygen isotope analyses to fluid inclusion homogenization temperatures on the same generation of quartz in complex banded veins to reveal the source and evolution of ore-forming fluids.

2. Geologic setting

The Te-rich Sandaowanzi and Te-poor Dong'an epithermal Au-Ag deposits that are the focus of this study are located in the eastern part of the Paleozoic Central Asian Orogenic Belt (CAOB) (Sengör et al. 1993; Jahn et al. 2000; Jahn 2004; Li 2006). It consists of the Erguna and Xing'an Blocks in the northwest, the Songliao Block in the central part and the Jiamusi Massif in the east, separated by the De'erbugan, Nenjiang-Hehei and Jiayin-Mudanjiang structures, respectively (Fig. 1a; Wu et al. 2007). Sandaowanzi is in the Xing'an Block and Dong'an is in the Songliao Block (Fig. 1a).

The Xing'an Block is dominated by Lower Cretaceous volcanic rocks (Ge et al. 2005; Sui et al. 2007; Zhang et al. 2010b; Gao et al. 2017, 2018a, b) and Neoproterozoic-Lower Cambrian metamorphic rocks, e.g., Luomahu Group (Qu 2008; Fig. 1a). Although sedimentation occurred during the Neoproterozoic and Paleozoic (Miao et al. 2004, 2007, 2015), metamorphism and deformation occurred in these blocks during the Jurassic (ca. 170-160 Ma; Miao et al. 2015). The Songliao Block is largely covered by Lower

Cretaceous volcanic rocks (Wang et al. 2002; Zhang et al. 2008) with local exposures of underlying granitoids and Precambrian rocks (Wu et al. 2000, 2001; Wang et al. 2006; Pei et al. 2007; Gao et al. 2007; Zhang et al. 2008) (Fig. 1a).

131

132

133

134

135

136

137

138

139

140

141

142

143

144

145

128

129

130

Regional structures mainly consist of NE- and NW-trending faults. The Nenjiang-Heihe fault and Jiayin-Mudanjiang fault control the distribution of gold deposits in the area (Fig. 1a). Mesoproterozoic intrusions contain inclusions of biotite-plagioclase-gneiss. Carboniferous intrusions consist of mylonitized diorite, tonalite and monzogranite. Early Permian intrusions are alkali-feldspar granites and Triassic-Jurassic intrusions consist of monzogranite and granodiorite (ca. 150-190 Ma; Sui et al. 2007; Gao et al. 2018b). Early Cretaceous intrusions consist of granite, granodiorite, and granite porphyry and have been dated at ca. 108-119 Ma (Gao et al. 2017, 2018b; Zhao et al., 2019). Although the ore ages are imprecise, Sandaowanzi, Dong'an and several other epithermal Au-Ag deposits in the area are interpreted to be coeval with a period of a ca. 108-122 Ma period of Early Cretaceous volcanism (Ge et al. 2005; Sui et al. 2007; Zhang et al. 2010a; Gao et al. 2017, 2018a, b). Epithermal Au-Ag mineralization and contemporaneous volcanism occurred in an extensional setting related to subduction of the Paleo-Pacific Plate (e.g., Wu et al. 2005b).

146

147

2.1. Sandaowanzi

Sandaowanzi produced 22 t Au at an average grade of 14 g/t, 127 t Ag at an average grade of 97 g/t, and 34 t Te at an average grade of 17 g/t from gold-bearing quartz veins hosted in early Cretaceous volcanic rocks (Yu et al. 2012; Xu et al. 2012; Liu et al. 2013; Zhai and Liu 2014; Gao et al. 2017). Sandaowanzi is hosted in the Lower Cretaceous Longjiang (121.7 Ma) Formation (Fm.). The lower and upper parts of the Longjiang Fm. contain pyroclastic- and lava flow-facies, respectively, with rock types comprising (brecciated) andesite and basaltic andesite. Geochemically, these igneous rocks are enriched in LREEs, Pb, K, and U, depleted in Nb, P, and Ti and are calc-alkaline (Gao et al. 2017). Major structures in the area include NW-SE and E-W-trending faults, with most deposits localized along NW-trending normal faults. The E-W-trending faults are earlier than the volcanism and crosscut Jurassic intrusive rocks (Fig. 1b). The main igneous intrusion in the area is the gray, medium-grained, Sandaowanzi monzogranite (177.2 Ma; Gao et al. 2017). Near ore deposits, Sandaowanzi monzogranite was emplaced under Longjiang Fm. andesite (Fig. 1b). Diabase dikes (116.6 Ma; Liu et al. 2011) crosscut the ore bodies. The major ore type at Sandaowanzi consists of Au-Ag-telluride-bearing quartz veins. Ore bodies (40 in three ore belts) occur along WNW-trending normal faults in andesite flows and pyroclastic breccias of the Lower Cretaceous Longjiang Fm. (Fig. 1b). Ore body II is the only current operating stope. The lenticular ore body is 213 m long and 0.8-14.3 m thick (averaging ~ 6 m). It strikes $20-40^{\circ}$, dips $58-77^{\circ}$, and plunges 520 m deep along the dip direction. The average Au grade of ore body II is 13.98 g/t (Gao et al. 2017).

149

150

151

152

153

154

155

156

157

158

159

160

161

162

163

164

165

166

167

168

Five stages have been identified in the veins (Fig. 2a-e). Telluride minerals in the deposit include calaverite, krennerite, sylvanite, petzite, hessite, stützite, empressite, altaite and coloradoite, which coexist with chalcopyrite, sphalerite, tetrahedrite, galena, native gold and minor pyrite and bornite (Fig. 4a). Other silver-bearing phases include acanthite, pyrargyrite, and kerargyrite. Petzite, sylvanite, calaverite and native gold assemblages generally occur in bonanza ore veins, and silver-bearing minerals occur mostly in the upper parts of the ore bodies (Yu et al. 2012). Gold-Ag tellurides are the major gold-bearing minerals (>95% of Au production); the remaining ~ 5% is in native gold. Alteration minerals include quartz, pyrite, sericite, carbonates, anhydrite, chlorite, and epidote. Pyrite, albite and chlorite are widespread in the alteration halo, which is ~15 m in width around the veins. Plagioclase is replaced by epidote, pyrite, calcite, sericite and chlorite. Other alteration minerals include pyrophyllite and minor siderite. Veins contain quartz, calcite and anhydrite with euhedral laumontite in vugs (Fig. 2f). Bulk oxygen isotope analyses indicate meteoric sources for the vein-forming fluids with $\delta^{18}O(Qz)$ ranging from -3.9 to -0.2, avg. -1.8 (Table 1; Wu et al. 2005a; Zhai et al. 2018). Sericite from the alteration halo yielded ⁴⁰Ar/³⁹Ar plateau, isochron, and total gas dates that overlap within error and yield a preferred age of 122.4 ± 3.9 Ma (Cheng 2017).

187

170

171

172

173

174

175

176

177

178

179

180

181

182

183

184

185

186

2.2. Dong'an

189

190

188

grade of 75.8 g/t from quartz-adularia veins hosted in early Cretaceous volcanic rocks. Stratigraphy at Dong'an includes Lower Cretaceous Guanghua Fm. volcanic rocks and Oligocene-Pliocene sandstone and conglomerate. The Guanghua Fm. consists predominantly of rhyolitic lava and rhyolitic tuff with minor dacitic lava that are underlain by an Early Jurassic coarse and fine-grained alkali feldspar granitic intrusion. The volcanic sequence and granitic intrusion are cut by granite porphyry dikes (Fig. 1c). The area is cut by a series of tensile-shear NS-, NE- and NNE-trending faults. The 14 gold orebodies recognized in the mine are controlled by NS- and NE-striking faults, dipping NW at 70 to 85°. Eight of the orebodies are hosted in rhyolitic lavas, five are hosted in rhyolitic porphyry dykes, and one is hosted in Jurassic granite. Gold-rich orebodies are commonly brecciated and the breccias are bounded by faults. The size of the gold veins varies considerably, from 50 to 800 m in length and 1 to 7 m in thickness. They extend to depths of less than 400 m and have grades from 3 to 10 g/t Au. The largest vein is 770 m long, 6.7 m thick on average, and has a vertical extent of 358 m, with an average grade of 8.8 g/t Au and 75.8 g/t Ag.

206

207

208

209

210

211

191

192

193

194

195

196

197

198

199

200

201

202

203

204

205

Ore minerals occur in sparse disseminations, local dense disseminations, isolated veinlets and stockworks inside the 1 to 7 m thick veins. Five stages have been identified in the veins (Fig. 3). Pyrite, galena, chalcopyrite, sphalerite, hematite, acanthite, native gold, electrum and native silver are present in the ores (Fig. 4b). Altaite, petzite, hessite and melonite are rare. Electrum (>95%) is the major gold- and silver-bearing mineral, with the

remaining ~5% in Au-Ag tellurides. Quartz, adularia, chlorite and calcite are the most abundant gangue minerals, with fluorite in places. The gold veins are enclosed by concentrically zoned alteration envelops consisting of quartz, chalcedonic quartz, sericite, adularia, chlorite, and pyrite. Bulk oxygen isotopes indicate meteoric sources for the veinforming fluids with, $\delta^{18}O(Qz)$ from -3.0 to 0.5, avg. -1.0 (Table 1; Ao et al. 2004; Yang 2008; Han 2013). Sericite yielded a $^{40}Ar/^{39}Ar$ date of 107.2 ± 0.6 Ma that is within uncertainty of a zircon U-Pb date of 108.1 ± 2.4 Ma on rhyolite porphyry (Zhang et al. 2010a).

3. Methods

3.1. Sampling and petrography

Samples used in this study were collected from vein exposures and drill holes in both vertical and horizontal directions at Sandaowanzi and Dong'an. The sample set includes barren and ore-bearing veins with different textures (Fig. 5; Table 2). Images of samples in reflected and transmitted light were obtained using petrographic microscope at the U.S. Geological Survey Denver Inclusion Analysis Laboratory. Thick sections (~200 µm) were used, because they are required for fluid inclusion studies. Although the birefringent colors of minerals in thick sections are different from standard thin sections under crossed polars, quartz textures are still evident. Representative samples were selected for

cathodoluminescence imaging.

3.2. SEM-CL and EDS

Cathodoluminescence (CL) images were acquired with a JEOL 5800LV scanning electron microscope (SEM) operated at 10 or 15 kV and approximately \sim 5 nA beam current at the U.S. Geological Survey Denver Microbeam Laboratory. Double polished thick sections (\sim 200 µm) and mineral mounts from 35 samples of banded vein material from Sandaowanzi and Dong'an were studied. The major element composition of adularia was determined by EDS with 50 mm² silicon drift detector on a FEI Quanta 450 FEG-SEM operated at 15 kV accelerating voltage. Beam calibration was performed on copper metal and Oxford factory standards. Orthoclase and albite standards were analyzed to check the calibration. The major element compositions of adularia were used to calculate SIMS bias corrections for δ^{18} O values.

3.3. Oxygen isotopes

The $\delta^{18}O$ values of quartz, chalcedony, and adularia from five representative samples were measured using a CAMECA IMS 1280 secondary ion mass spectrometer (SIMS) at the WiscSIMS Laboratory, University of Wisconsin-Madison (Kita et al. 2009; Valley and Kita 2009; Heck et al. 2011). Oxygen isotope ratios were analyzed using a 1.6 nA $^{133}Cs^+$

primary beam of ions focused to a spot of ~10 µm diameter. Analysis pits were 1-2 µm deep. Ions of ¹⁶O⁻ and ¹⁸O⁻ were simultaneously collected in two movable Faraday cup detectors with an average ¹⁶O⁻ intensity of 2.7 × 10⁹ cps and ¹⁶O¹H⁻ was collected in the axial Faraday cup to check for traces of water in quartz. The magnetic field strength was held stable using a nuclear magnetic resonance (NMR) probe, which was readjusted every 12 h. The mass resolving power (MRP=M/ Δ M), measured at 10% peak height, for δ^{18} O analytical conditions was ~2200 for the movable Faraday detectors and ~5000 for the axial position, allowing ¹⁶O¹H⁻ to be resolved from ¹⁷O⁻ (Kita et al. 2009; Wang et al. 2014). Each spot analysis took approximately 4 min, which includes 10 s of presputtering to penetrate the gold coating, ~60 s to stabilize sputtering and automatically center the secondary ions in the field aperture and 80 s (20 cycles of 4 s each) to integrate secondary ions. Detailed descriptions of these analytical conditions and the instrument setup at WiscSIMS have been published previously (Kelly et al. 2007; Kita et al. 2009; Valley and Kita 2009; Heck et al. 2011; Wang et al. 2014). All data were collected with a standardsample-standard bracketing procedure of four UWQ-1 quartz-standard measurements, 10-16 sample measurements and four UWQ-1 standard measurements. Oster et al. (2017) show that the SIMS bias is not measurably different for UWQ-1 that is an anhydrous quartz vs. the hydrous opal standard, BZVV. Bracketing standards were used to evaluate the reproducibility of a series of measurements as well as to correct for the instrumental bias and minor instrument drift. The external spot-to-spot reproducibility of bracketing standards averaged $\pm 0.22\%$ (2SD) for oxygen isotope analyses. Raw values of isotope

254

255

256

257

258

259

260

261

262

263

264

265

266

267

268

269

270

271

272

273

274

ratios measured by SIMS were corrected to the VSMOW scale for oxygen based on values measured for the UWQ-1 bracketing standards (UWQ-1: $\delta^{18}O = 12.33\%$, VSMOW, Kelly et al. 2007; Heck et al. 2011). To ensure that the best precision and accuracy were achieved, all analyses were conducted on spots within 5 mm of the center of a polished 25 mm mount (Kita et al. 2009; Peres et al. 2013).

Four feldspar reference materials, Amelia Ab (Or% = 0), MES-4 (Or% = 71), FCS (Or% = 75) and Gem28 (Or% = 93), were measured in the same SIMS session to determine the bias as a function of major element chemistry (Pollington 2013). Because we use UWQ-1 as a bracketing standard, all calculations use the difference in the biases of quartz and feldspar to calculate VSMOW values of feldspar (adularia) (Pollington 2013). Relative bias to UWQ-1 of Amelia Ab was 3.87% for end member albite during the analysis session. The relative biases of FC, MES-4 and Gem28 were 4.76, 4.98 and 4.94% for K-feldspar (Appendix A). The mean measured UWQ-1 values are 5.94 for SG-1, 5.82 for SG-2, and 5.98 for SG-3, respectively. All measured feldspars (adularia) were measured with SG-3.

Values of ¹⁶O¹H⁻/¹⁶O⁻ (OH/O hereafter) were background corrected for contaminant OH by subtracting the average OH/O values measured on bracketing analyses of UWQ-1 quartz standard, that comes from a granulite facies quartzite and is assumed to be anhydrous (see Wang et al. 2014). Background corrected ratios of OH/O are not calibrated against a standard, but are useful on a relative basis to identify subtle changes in OH content

of silica (e.g., chalcedony) as well as aqueous solid and fluid inclusions.

3.4. Microthermometry

In each of the five representative samples, fluid inclusion assemblages observed in crystalline quartz were spatially correlated with the CL bands analyzed by SIMS. Fluid inclusion petrography and microthermometry were conducted at the U.S. Geological Survey Denver Inclusion Analysis Laboratory. A Linkman 600 heating/freezing stage on an Olympus BX60 microscope was used to measure the ice melting temperature and homogenization temperature of fluid inclusions in each assemblage. A pure H_2O standard with an ice melting temperature (T_m) of 0 °C and a critical homogenization temperature (T_m) of 373.6 °C was used to calibrate the stage with the data reproducible to ± 0.2 °C for ice melting temperatures and ± 2.0 °C for homogenization temperatures.

4. Results

4...1 Petrography of minerals

In this study, we describe quartz textures using terminology from Dong et al. (1995) for adularia-sericite epithermal deposits. Colloform (Fig. 6a-e), jigsaw (Fig. 6b), bladed (Fig. 7a), flamboyant (Fig. 7b), plumose (Fig. 7c), granoblastic and comb (Fig. 6c-e)

textures were observed under crossed polars. Other textures such as zonal and cockade are evident on SEM-CL images.

At Sandaowanzi, colloform textures (Stage I) are barren of gold and consist of alternating bands of fine-grained quartz with a jigsaw texture and thin layers of quartz with a granoblastic texture (Fig. 6a, b). In thin section, jigsaw texture is characterized by aggregates of microcrystalline to coarse crystalline quartz crystals with interpenetrating grain boundaries (Fig. 6a, b). Fibrous chalcedony with sweeping extinction and a botryoidal texture (Stage II) also grows on, or is mantled by, quartz with a granoblastic texture (Fig. 6c). Intervening quartz layers with granoblastic and comb textures (Stage III; Fig. 6d, e) usually contain sparse liquid-rich fluid inclusions. Gold-silver telluride bands are associated with a thin overgrowth (Stage IV) on comb quartz (Fig. 6c-e).

At Dong'an, bladed texture (Stage I) consists of chalcedony and crystal quartz (Fig. 7a). Flamboyant texture (Stage II) followed by Stage III quartz and chalcedony, contains three dimensional arrays of small liquid- and vapor-rich inclusions that follow crystallographic axes (Fig. 7b). Plumose texture (Stage IV; Fig. 7c) consists of quartz and chalcedony overgrowths on euhedral adularia (Stage IV; Fig. 7d, e). Colloform textures (Stage IV) are usually mineralized and consist of alternating bands of fine-grained quartz, coarse-grained quartz, chalcedony, and fine-grained adularia with electrum, pyrite, and sphalerite +/- trace amounts of Au-Ag tellurides (Fig. 7d, e, f).

4.2. Cathodoluminescence of minerals

Cathodoluminescence (CL) images were used to further document the paragenetic relationships among, textures of, and zoning within quartz, chalcedony, adularia and other gangue and ore minerals. The CL images shown in Figures 8 and 9 are of the thick sections that we used for SIMS δ^{18} O and fluid inclusion analyses. Textural complexity is clearly evident. In each panel, the white arrows show the direction of mineral growth with stages indicated by Roman numerals. Barren and high-grade material collected from the Sandaowanzi quartz-telluride veins is shown on Figures 8a-e and Dong'an quartz-adularia-electrum veins on Figures 9a-c. Granoblastic and comb quartz is CL-gray (Fig. 8a and b), CL-dark or CL-bright (Fig. 8d and e), whereas chalcedony is homogeneous and CL-dark (Fig. 8b and c). Adularia is also homogeneous and CL-dark relative to quartz (Fig. 9b and c). The multiple generations of quartz identified by CL at Sandaowanzi and Dong'an were grouped into 5 stages based on cross-cutting relationships, growth zones, and mineral assemblages as described below.

At Sandaowanzi, the paragenetic sequence is: (I) fine-grained quartz + coarse-grained quartz, (II) chalcedony + CL-gray quartz + CL-dark quartz + CL-bright quartz, (III) CL-gray comb quartz + CL-dark zonal quartz, (IV) CL-bright quartz + CL-dark quartz + Au-Ag-tellurides, (V) thin veinlets of CL-bright quartz (Fig. 8). Colloform textures are

common at Sandaowanzi, and many are barren (Fig. 8a). Stage I has a colloform texture consisting of alternating fine-grained and coarse-grained quartz bands (Fig. 8a). Fine-grained quartz has a jigsaw texture in thin section, is CL-dark, and lacks fluid inclusions. Coarse-grained quartz is generally CL-gray and contains sparse tiny fluid inclusions. In high-grade veins, Stage I colloform quartz is sometimes brecciated and overgrown by Stage II chalcedony and crystalline quartz (e.g., Fig. 8b). In some sections, Stage II chalcedony forms circles that are overgrown by quartz (Fig. 8c). Stage III quartz consists of CL-gray comb and CL-dark zones that are overgrown by a Stage IV thin rim of CL-bright and dark quartz followed by Au-Ag-tellurides (Fig. 8c-e). Thin, (20 ~ 120 μm in width) Stage V veinlets of CL-bright quartz are also present that cross cut the early stages (e.g., Fig. 8b). Fluid inclusions are present in Stages I, II and III CL-gray and CL-bright quartz crystals.

At Dong'an, the paragenetic sequence is: (I) bladed chalcedony + bladed quartz, (II) CL-dark quartz + CL-bright quartz, (III) chalcedony + CL-gray quartz + CL-bright quartz, (IV) adularia + chalcedony + CL-dark quartz + CL-gray quartz + electrum, and (V) thin veinlets of CL-dark and bright quartz (Fig. 9). Bladed quartz textures including ghost and lattice are common at Dong'an, and many are barren. Both chalcedony and bladed Stage I quartz are CL-dark, whereas Stage II and III quartz are both CL-bright and CL-dark and can have a circular shape (Fig. 9a). Stage II quartz is sometimes brecciated and overgrown by Stage III of chalcedony, CL-gray and CL-bright quartz with a cockade texture (e.g., Fig. 9b). In ore-bearing veins, earlier stages of quartz are typically brecciated and cemented

with Stage IV adularia (Fig. 9b and c). Stage IV adularia is overgrown by chalcedony, CL-dark quartz and CL-gray comb quartz followed by electrum (Fig. 9c). Stage V veinlets of quartz are also present that cross-cut the Stage II, III and IV quartz bands (Fig. 9b and c). Stages I, II and IV quartz contain fluid inclusions.

4.3. SIMS oxygen isotopes

SIMS oxygen isotope analyses of quartz, chalcedony and adularia from three samples at Sandaowanzi and two samples at Dong'an are presented in Appendix A, and displayed on Figures 8-10. Sandaowanzi quartz and chalcedony have a wide range of δ^{18} O values from -7.1 to +7.7‰. There is a slight decrease from Stage I to Stage III followed by an abrupt increase in Stage IV quartz, which is mantled by Au-Ag-tellurides (Fig. 10). At Dong'an, quartz and chalcedony have a narrow range from -2.2 to +1.6‰ and adularia varies from -5.9 to -3.5‰ (Fig. 10).

In Stage I barren colloform texture quartz at Sandaowanzi, $\delta^{18}O$ values fluctuate mildly along the direction of growth (Fig. 8a). Bands of fine-grained quartz (FQ, blue symbols) have $\delta^{18}O$ values that are 1-2‰ higher than those of more coarsely crystalline quartz (red symbols) (Fig. 8a). In contrast, the $\delta^{18}O$ values of Stage II CL-gray quartz and chalcedony are 3-4‰ lower than brecciated Stage I fine-grained quartz (Fig. 8b and c). Stage III CL-gray comb quartz also has $\delta^{18}O$ values that are 1-2‰ lower than Stage II CL-bright and

CL-gray quartz and chalcedony (Fig. 8d and e). Notably, the Stage II quartz and chalcedony and Stage III CL-gray comb quartz have much lower $\delta^{18}O$ values (down to -7.1‰) than the rims of Stage IV CL-dark and CL-bright quartz followed by tellurides (e.g., Fig. 8d and e). The Stage V thin quartz veinlet has an $\delta^{18}O$ value of -2.4‰ (e.g., Fig. 8b).

In Stage I to Stage III barren ghost bladed textures at Dong'an, $\delta^{18}O$ values fluctuate from -2.2 to +1.6% with a median of -0.3% (Fig. 9a). In Stage II to Stage III silica bands with a cockade texture, $\delta^{18}O$ values have a narrow range from -2.1 to -0.2% (Fig. 9b). In ore-bearing veins, the $\delta^{18}O$ values of Stage IV quartz followed by electrum have a narrow range from -1.6 to -0.2% (Fig. 9c) that is within the range of values from the barren bands (Stage I to Stage III). Moreover, the Stage V thin quartz veinlet cross cutting silica bands and cockade texture also has $\delta^{18}O$ values from -1.1 to -0.1% that are similar to the other stages (Fig. 9b and c).

4.4. Fluid inclusion microthermometry

Fluid inclusion petrography and microthermometry were conducted on the same samples used for CL imaging and SIMS analysis, which enabled spatial correlation of homogenization temperatures with the δ^{18} O results obtained on specific bands of quartz. Fluid inclusions were only observed in crystalline quartz and they are uncommon (Fig. 11). None were observed in fine-grained quartz or chalcedony. Microthermometric

measurements were generally made on inclusions more than 5 µm in diameter. Most of the inclusions were classified as primary; they have irregular shapes, occur along crystal growth zones, and are liquid-rich with 0 to 25 vol\% vapor at room temperature. Secondary inclusions along fractures are also liquid-rich. No vapor-rich inclusions were found. Thus, the primary liquid-rich inclusions in crystal quartz were trapped prior to, or between, episodes of boiling. Microthermometric measurements on liquid-rich inclusions from each band are summarized in Table 3. All of the liquid-rich inclusions are dilute with salinities between 0 and 1.0 wt.% NaCl equiv. The homogenization temperatures (T_h) of primary liquid-rich inclusions vary from 237 to 281 °C (Fig. 12) and have higher temperatures than those of secondary inclusions with T_h from 164 to 216 °C. Entrapment temperature is equaled to homogenization temperature because of low pressure in epithermal systems. To evaluate this further, the pressure-corrected temperatures at the conditions of T_h=250 °C and T_m=-0.5 °C are 251, 255, and 259 °C with the referred pressures of 50, 100, and 150 bars (Steele-MacInnis et al., 2012).

436

437

438

439

440

441

442

422

423

424

425

426

427

428

429

430

431

432

433

434

435

At Sandaowanzi, fluid inclusions in a band of Stage I quartz with barren colloform texture has a narrow range of high T_h from 268.6 to 270.2 °C (average 269.4 °C); three groups of secondary fluid inclusions with lower T_h are also present (Table 3). Stage II CL-bright quartz has a T_h range from 248.6 to 252.4 °C (avg. 250.9 °C). Fluid inclusions in two bands of Stage III CL-gray quartz have a narrow range of T_h with averages of 248.2 °C and 250.5 °C. The low $\delta^{18}O$ of fluids in equilibrium with such quartz suggest that it

precipitated from exchanged meteoric water. In contrast, fluid inclusions in Stage III comb quartz followed by the Stage IV rim associated with Au-Ag-tellurides have higher average T_h values of 276.2, 266.4 and 277.5 °C (Table 3) and the $\delta^{18}O$ values of fluids in equilibrium with the Stage IV rim are much higher.

At Dong'an, fluid inclusions in Stage I quartz with a ghost bladed texture also have high T_h from 267.6 to 269.5 °C (avg. 268.6 °C) (Table 3). This temperature may be representative of fluids prior to boiling. Fluid inclusions in Stage II CL-bright quartz layers in colloform texture have T_h from 242.1 to 245.0 °C (avg. 243.4 °C). Similarly, the T_h of fluid inclusions in Stage IV CL-gray comb quartz followed by electrum vary between 237.2 and 255.7 °C (avg. 244.6 °C), and between 244.2 and 248.9 °C (avg. 246.6 °C) (Table 3), which are within the range of data from barren bands. These data indicate that the quartz and adularia bands associated with electrum precipitated at average temperatures, which is unlike Sandaowanzi.

5. Discussion

Box and whisker plots showing the $\delta^{18}O$ values of each stage of chalcedony, quartz, and adularia from Sandaowanzi and Dong'an are compared to one another on Figure 10 and discussed below. Both Sandaowanzi and Dong'an have similar initial $\delta^{18}O(Qz)$ values (~0‰, Stage-I) and fluid inclusion homogenization temperatures (~270 °C). These initial

fluids ($\delta^{18}O(H_2O) = -8.6\%$, Stage-I) are indicative of isotopically exchanged meteoric water (e.g., Hedenquist and Lowenstern 1994; Simmons 1995; John et al. 2003; Simmons et al. 2005) and are typical of most other adularia-sericite Au-Ag deposits in the world (e.g., Simmons 1995; Faure et al. 2002; John et al. 2003). The magmatic fluid signal is thought to be weak in these deposits, because the intrusive source is deep such that magmatic fluids are diluted by a much larger volume of meteoric water (e.g., Giggenbach 1992; Hedenquist and Lowenstern 1994; Simmons 1995; Simmons et al. 2005).

At Sandaowanzi, variations in the $\delta^{18}O$ of quartz from ~0% in Stage I, to ~-4% in Stage II, to ~-6% in Stage III, to ~+7% in Stage IV, to ~-3% in Stage V (Fig. 10) show that, at the μ m to mm scale only accessible by SIMS (10- μ m spots), there is a 15% fluctuation in $\delta^{18}O$. We infer that this fluctuation reflects a step change in the proportions of meteoric and magmatic and fluid in the veins (Fig. 10). Evidence for the mixing of meteoric water with magmatic fluids is provided by the low $\delta^{18}O$ values of Stage II-III quartz, the high $\delta^{18}O$ value of Stage IV quartz followed by Au-Ag-tellurides and the low $\delta^{18}O$ values of Stage V quartz veins (Fig. 10). The abrupt positive $\delta^{18}O$ shift (up to +7.7) detected in Stage IV quartz followed by Au-Ag telluride minerals at Sandaowanzi (Figs. 8c-e and 10) is similar to those attributed to input of magmatic fluids or vapors in other deposits (Giggenbach 1992; Hedenquist and Lowenstern 1994; Simmons 1995; Spry et al. 1996; Taylor 1997; Hedenquist et al. 1998; Simmons et al. 2005; Christie et al. 2007; Saunders et al. 2008; Simpson and Mauk 2011; Simmons et al. 2016).

486

487

488

489

490

491

492

493

494

495

496

497

498

499

500

501

502

503

504

505

Regarding ore-forming processes at Sandaowanzi, (i) colloform quartz veins (Stage I) are typical textures that form from boiling fluids and are thought to be a product of flashingintense episodic boiling where the majority of the liquid transforms to steam (Moncada et al. 2012; Shimizu 2014; Simpson et al. 2015; Taksavasu et al. 2018). Layers of chalcedony and fine-grained quartz with a jigsaw texture are thought to form by recrystallization of an amorphous silica precursor that precipitated during episodes of boiling (Fournier 1985; Saunders 1990 1994; Herrington and Wilkinson 1993; Saunders and Schoenly 1995; Shimizu et al. 1998; John et al. 2003; Shimizu 2014; Prokofiev et al. 2016). The small decrease in oxygen isotope ratios from Stage I to III indicates that hydrothermal fluids were still dominated by meteoric water (Fig. 10). (iii) The subsequent increase by up to 15% during Stage IV records a substantial input of magmatic fluids into the veins. The euhedral comb textures of Stage III and IV quartz are unlike typical textures that form from boiling fluids (e.g., bladed quartz, Dong et al. 1995; Moncada et al. 2012), which suggests that they precipitated from slowly changing conditions, such as fluid mixing or gentle boiling (a relatively small portion of the liquid mass is transferred to the vapor phase) or nonboiling (Fournier 1985; Dong et al. 1995; Moncada et al. 2012; Shimizu 2014; Taksavasu et al. 2018). Fluid inclusions in Stage III quartz (~280 °C) followed by the Stage IV rim have higher homogenization temperatures than those in Stage II quartz (~250 °C). (iv) After Stage IV magmatic fluid input, Stage V quartz δ^{18} O values decrease to -2.8%, which reflects dilution by meteoric water with a calculated $\delta^{18}O(H_2O)=-12.3\%$.

Although the positive oxygen isotope shift in Stage IV quartz could theoretically be explained by intense boiling with rapid cooling and oxygen isotope exchange with host rocks, textures (e.g., bladed quartz) with fluid inclusions (e.g., coexisting vapor-rich and liquid-rich) that form from boiling fluids are absent, and host rocks were sealed off by earlier stages of quartz. Fluid inclusion data also show that temperature increased (from 250 to 280 °C) in comb quartz followed by tellurides, which indicates that the positive oxygen isotope shift (15‰) was accompanied by heating rather than cooling. Furthermore, if the fluid moved through underlying metasedimentary rocks, they are unlikely to leach significant amounts of Te because of the low Te concentration in the crust (5 ppb; Wedepohl 1995). In addition, the subaerial continental setting of NE China in the Early Cretaceous precludes involvement of seawater in the hydrothermal systems. Thus, the abrupt positive shift in δ^{18} O values in Stage IV quartz and the ensuing precipitation of Au-Ag telluride minerals must be due to a significant input of magmatic fluid.

To evaluate this further, the mixing ratios between hot (300, 325, and 350°C) magmatic water and cooler 250°C exchanged meteoric water required to produce a shift from Stage III (average -5‰) to Stage IV (max +7.7‰), are ~1.7/1, ~1.9/1 and ~2.2/1 at corresponding temperatures of 281, 299 and 318 °C (Fig. 13). These results show that mixing with 300°C magmatic fluids is required to explain the δ^{18} O(Qz) shift from -5 to 7.7‰ and the maximum temperature of ~278 °C recorded by fluid inclusions. Higher

temperature magmatic fluids produce the same isotopic shift at much higher temperatures. Magmatic fluid must have been saturated with dissolved silica because it cooled from magmatic temperatures to 300°C before mixing with 250°C exchanged meteoric water. Because the difference in silica solubility between 300°C magmatic fluid and 250°C exchanged meteoric water is small only a small amount of quartz precipitated followed by tellurides. The magmatic fluid must also have had a low salinity or the increase in temperature would have been accompanied by a marked increase in salinity, which is not observed. We therefore surmise that the magmatic fluid in this system consisted of low salinity condensed magmatic vapor with elevated Te, Au, and Ag contents, as postulated by Williams-Jones and Heinrich (2005).

At Dong'an, although five stages of quartz were also distinguished, the δ^{18} O values of quartz and chalcedony are much more consistent with a narrow range of -2.2 to +1.6‰ that is indicative of meteoric hydrothermal fluids (Fig. 10). Although adularia has a lower range from -5.9 to -3.5‰ (Fig. 10), this difference is mostly due to the ~3‰ fractionation factor between quartz and K-feldspar at epithermal conditions (Clayton et al. 1972, 1989; Chiba et al. 1989). In other words, adularia precipitated from the same fluid as quartz and chalcedony.

Regarding ore-forming processes at Dong'an, (i) Stage I bladed quartz is a pseudomorphic replacement of bladed calcite that formed by boiling of meteoric water

(Simmons and Christenson 1994; Dong et al. 1995; Etoh et al. 2002a) and has oxygen isotope values that fluctuate over a range of ~2.0%. Stage II flamboyant texture followed by Stage III quartz and chalcedony also forms from boiling fluids (Bodnar et al. 1985; Dong et al. 1995) and oxygen isotope compositions did not change much during precipitation of Stage II and III quartz and chalcedony. (iii) Subsequent boiling during Stage IV was accompanied by an increase in pH and precipitation of quartz, adularia, calcite, electrum, sphalerite and galena with plumose and colloform textures (Reed 1982; Reed and Spycher 1985; Simmons and Browne 2000; Zhou et al. 2001; Etoh et al. 2002b; Shimizu 2014). Gold-Ag tellurides are notably rare or absent. Fluid inclusions in Stage IV quartz also have homogenization temperatures that are similar to those in Stage II quartz (~245°C). (iv) Finally, although there is no obvious oxygen isotope evidence for inputs of magmatic fluid, the trace amount of Au-Ag telluride minerals allows that there may have been minute inputs. (Fig. 7f). These results confirm that boiling was the main mechanism of Au-Ag mineralization in Stage IV quartz-adularia-electrum bands at Dong'an, which is also similar to other adularia-sericite Au-Ag deposits in the world (e.g., Hishikari, Japan; Hayashi et al. 2001; Faure et al. 2002).

564

548

549

550

551

552

553

554

555

556

557

558

559

560

561

562

563

6. Implications

566

567

568

565

This study shows that detailed understanding of the textures, oxygen isotope compositions, homogenization temperatures and salinities of fluid inclusions within

paragenetically complex quartz veins can advance understanding of fluid sources and processes of mineral precipitation in Au-Ag \pm Te bearing epithermal systems. The detailed CL patterns, oxygen isotope and temperature variations documented in these quartz veins show that inputs of magmatic fluid into adularia-sericite epithermal systems are exceedingly difficult to detect without in-situ micro analysis spatially correlated to textures. Furthermore, these minerals only record clear evidence of magmatic inputs in thin growth zones of quartz (20-100 µm) that are mantled by Au-Ag-Te minerals. Consequently, most of the evidence gathered from gangue minerals in these systems using conventional methods is apt to record convection and episodic boiling of more or less barren meteoric hydrothermal fluids. Our results support a growing body of evidence that productive highgrade Au-Ag-telluride ores in adularia-sericite epithermal systems form by the input of magmatic fluids into otherwise barren meteoric flow systems. This interpretation is consistent with that proposed to explain the origin of bonanza epithermal Au-Ag deposits in the Northern Great Basin, USA based on the O and S isotope compositions of ore and gangue minerals (Saunders et al., 2008), and thus may have broad applicability.

584

569

570

571

572

573

574

575

576

577

578

579

580

581

582

583

Acknowledgements

586

587

588

589

585

The authors are grateful to the Bureau of Geology and Mineral Exploration (Heilongjiang), the Geological Brigades of the Heilongjiang Geological Survey, and Sandaowanzi and Dong'an Gold Co. Ltd. for their whole-hearted support of the field work.

Drs. Le Wang and Kaixuan Hui are thanked for their help on the sample collection. Drs. Richard J. Moscati, Thomas Monecke, Benjamin J. Linzmeier and Mitchell Bennett are thanked for their help on the sample preparation, CL images, QGIS maps and FIs homogenization temperatures. The manuscript benefited from reviews by James A. Saunders, an anonymous referee, and the USGS reviewers Craig A. Johnson and Jeffrey L. Mauk. This study was funded by the Natural Science Foundation of China (Grant No. 41802099), the National Key Research and Development Program of China (Grant No. 2017YFC0601306), the foundation of the Key Laboratory of Mineral Resources, IGGCAS (Grant No. KLMR2017-08), the CPSF-CAS Joint Foundation for Excellent Postdoctoral Fellows (Grant No. 2017LH016), and the China Postdoctoral Science Foundation (Grant No. 2018M631567). WiscSIMS is supported by the U.S. National Science Foundation (EAR-1658823) and the University of Wisconsin- Madison. JWV and KK are supported by the U.S. Department of Energy, Office of Science, Office of Basic Energy Sciences (Geosciences) under Award Number DE-FG02-93ER14389. Any use of trade, product, or firm names is for descriptive purposes only and does not imply endorsement by the U.S. Government.

606

605

590

591

592

593

594

595

596

597

598

599

600

601

602

603

604

References cited list

608

609

610

607

Ahmad, M., Solomon, M., and Walshe, J. (1987) Mineralogical and geochemical studies of the Emperor gold telluride deposit, Fiji. Economic Geology, 82, 345–370.

- Anderson, W.B., and Eaton, P.C. (1990) Gold mineralization at the Emperor Mine,
- Vatukoula, Fiji. Journal of Geochemical Exploration, 36, 267–296.
- Ao, G., Xue, M., Zhou, J., Wang, G., and Chen, H. (2004) Genesis of Dong'an gold deposit,
- Heilongjiang province, NE China. Mineral Resources and Geology, 18, 118–121 (in
- 615 Chinese with English abstract).
- Beaty, D.W., Kelley, K.D., Silberman, M.L., and Thompson, T.B. (1996) Oxygen isotope
- geochemistry of a portion of the Cripple Creek hydrothermal system, Guidebook
- Series, Society of Economic Geologists, Inc., 26, 55–64.
- Bodnar, R.J., Reynolds, T.J., and Kuehn, C.A., 1985, Fluid-inclusion systematics in
- epithermal systems, in Berger, B.R., and Bethke, P.M., ed., Geology and Geochemistry
- of Epithermal Systems, Society of Economic Geologists, Inc., p. 73–97.
- 622 Cernuschi, F., Dilles, J.H., Grocke, S.B., Valley, J.W., Kitajima, K., and Tepley, F.J. III
- 623 (2018) Rapid formation of porphyry copper deposits evidenced by diffusion of oxygen
- and titanium in quartz. Geology, 46, 611–614.
- 625 Cheng, L. (2017) Ore genesis of the Sandaowanzi telluride-gold deposit in Heilongjiang
- province. M.Sc. thesis, Changchun, China, Jilin University, 36–38 (in Chinese with
- English abstract).
- 628 Chiba, H., Chacko, T., Clayton, R.N., and Goldsmith, J.R. (1989) Oxygen isotope
- fractionations involving diopside, forsterite, magnetite, and calcite: Application to
- geothermometry. Geochimica et Cosmochimica Acta, 53, 2985–2995.
- 631 Christie, A.B., Simpson, M.P., Brathwaite, R.L., Mauk, J.L., and Simmons, S.F. (2007)

- Epithermal Au-Ag and Related Deposits of the Hauraki Goldfield, Coromandel
- Volcanic Zone, New Zealand. Economic Geology, 102, 785–816.
- 634 Ciobanu, C.L., Cook, N.J., and Spry, P.G. (2006) Preface Special Issue: Telluride and
- selenide minerals in gold deposits how and why?. Mineralogy and Petrology, 87,
- 636 163–169.
- 637 Clayton, R.N., Goldsmith, J.R., and Mayeda, T.K. (1989) Oxygen isotope fractionation in
- 638 quartz, albite, anorthite, and calcite. Geochimica et Cosmochimica Acta, 53, 725–733.
- 639 Clayton, R.N., O'Neil, J.R., and Mayeda, T.K. (1972) Oxygen isotope exchange between
- quartz and water. Journal of Geophysical Research, 77, 3057–3067.
- 641 Cook, N.J., and Ciobanu, C.L. (2005) Tellurides in Au deposits: implications for modelling,
- in Proceedings Mineral Deposit Research. Meeting the Global Challenge 2005,
- 643 Springer, 1387–1390.
- 644 Cook, N.J., Ciobanu, C.L., Spry, P.G., and Voudouris, P. (2009) Understanding gold-
- (silver)-telluride-(selenide) mineral deposits. Episodes, 32, 249–263.
- 646 Cooke, D.R., and McPhail, D. (2001) Epithermal Au-Ag-Te mineralization, Acupan,
- Baguio district, Philippines: numerical simulations of mineral deposition. Economic
- Geology, 96, 109–131.
- Dong, G., Morrison, G., and Jaireth, S. (1995) Quartz textures in epithermal veins,
- Queensland; classification, origin and implication. Economic Geology, 90, 1841–1856.
- Etoh, J., Izawa, E., and Taguchi, S. (2002b) A fluid inclusion study on columnar adularia
- from the Hishikari low-sulfidation epithermal gold deposit, Japan. Resource Geology,

- 653 52, 73–78.
- Etoh, J., Izawa, E., Watanabe, K., Taguchi, S., and Sekine, R. (2002a) Bladed quartz and
- its relationship to gold mineralization in the Hishikari low-sulfidation epithermal gold
- deposit, Japan. Economic Geology, 97, 1841–1851.
- Faure, K., Matsuhisa, Y., Metsugi, H., Mizota, C., and Hayashi, S. (2002) The Hishikari
- Au-Ag epithermal deposit, Japan: oxygen and hydrogen isotope evidence in
- determining the source of paleohydrothermal fluids. Economic Geology, 97, 481–498.
- Fekete, S., Weis, P., Driesner, T., Bouvier, A.S., Baumgartner, L., and Heinrich, C.A.
- 661 (2016) Contrasting hydrological processes of meteoric water incursion during
- magmatic-hydrothermal ore deposition: An oxygen isotope study by ion microprobe.
- Earth and Planetary Science Letters, 451, 263–271.
- Fournier, R.O. (1985) The behavior of silica in hydrothermal solution, in Berger, B.R., and
- Bethke, P.M., ed., Geology and Geochemistry of Epithermal Systems. Society of
- Economic Geologists, Inc., 45–61.
- 667 Friedman, I., and O'Neil, J.R. (1977) Compilation of stable isotope fractionation factors of
- geochemical interest, in Fleisher, M., ed., Data of Geochemistry (Sixth Edition):
- United States Government Printing Office, Washington, U.S. Geological Survey
- 670 Professional Paper 440–KK.
- 671 Gao, F.H., Xu, W.L., Yang, D.B., Pei, F.P., Liu, X.M., and Hu, Z.C. (2007) LA-ICP-MS
- zircon U-Pb dating from granitoids in southern basement of Songliao basin:
- Constraints on ages of the basin basement. Science in China (Series D), 50, 995–1004.

- Gao, S. (2017) Study on Mesozoic gold metallogenic system, northern Heihe, Heilongjiang
- province. Ph.D. thesis, Beijing, China, China University of Geosciences (Beijing), 196
- 676 (in Chinese with English abstract).
- Gao, S., Xu, H., Quan, S.L., Zang, Y.Q., Wang, T. (2018b) Geology, hydrothermal fluids,
- H-O-S-Pb isotopes, and Rb-Sr geochronology of the Daxintun orogenic gold deposit
- in Heilongjiang province, NE China. Ore Geology Reviews, 92, 569–587.
- Gao, S., Xu, H., Zang, Y.Q., and Wang, T. (2018a) Mineralogy, ore-forming fluids and
- geochronology of the Shangmachang and Beidagou gold deposits, Heilongjiang
- province, NE China. Journal of Geochemical Exploration, 188, 137–155.
- Gao, S., Xu, H., Zang, Y.Q., Yang, L.J., Yang, B., and Wang, T. (2017) Late Mesozoic
- magmatism and metallogeny in NE China: The Sandaowanzi-Beidagou example.
- International Geology Review, 59, 1413–1438.
- 686 Ge, W.C., Wu, F.Y., Zhou, C.Y., and Zhang, J.H. (2005) Zircon U-Pb ages and its
- significance of the Mesozoic granites in the Wulanhaote Region, central Great Xing'an
- Range. Acta Petrologica Sinica, 21, 749–762 (in Chinese with English abstract).
- 689 Giggenbach, W.F. (1992) Magma degassing and mineral deposition in hydrothermal
- systems along convergent plate boundaries. Economic Geology, 87, 1927–44.
- 691 Goldfarb, R.J., Berger, B.R., George, M.W., and Seal, R.R., II (2017) Tellurium, in Schulz,
- K.J., DeYoung, J.H., Jr., Seal, R.R., II, and Bradley, D.C., eds., Critical Mineral
- Resources of the United States—Economic and Environmental Geology and Prospects
- for Future Supply. U.S. Geological Survey Professional Paper 1802, R1–R27.

- 695 Goldfarb, R.J., Hofstra, A.H., Simmons, S.F. (2016) Critical elements in Carlin, epithermal,
- and orogenic gold deposits, in Verplanck, P.L., and Hitzman, M.W., eds., Rare Earth
- and Critical Elements in Ore Deposits. Society of Economic Geologists, Inc., 217–244.
- Han, S. (2013) Magmatic fluids and gold mineralization of the Late Mesozoic epithermal
- gold system in northern Lesser Xing'an Range, NE China. Ph.D. dissertation,
- 700 Changchun, China, Jilin University, 47–50 (in Chinese with English abstract).
- Haroldson E.L., Brown P.E., Ishida A., and Valley J.W. (2020) SIMS oxygen isotopes
- indicate Phanerozoic fluids permeated a Precambrian gold deposit. Chemical Geology,
- 703 533, 119429.
- Hayashi, K.I., Maruyama, T., and Satoh, H. (2001) Precipitation of gold in a low-
- sulfidation epithermal gold deposit: Insights from a submillimeter-scale oxygen
- isotope analysis of vein quartz. Economic Geology, 96, 211–216.
- Heck, P.R., Huberty, J.M., Kita, N.T., Ushikubo, T., Kozdon, R., and Valley, J.W. (2011)
- SIMS analyses of silicon and oxygen isotope ratios for quartz from Archean and
- 709 Paleoproterozoic banded iron formations. Geochimica et Cosmochimica Acta, 75,
- 710 5879–5891.
- Hedenquist, J.W., and Lowenstern, J.B. (1994) The role of magmas in the formation of
- hydrothermal ore deposits. Nature, 370, 519–527.
- Hedenquist, J.W., Arribas, A. Jr., and Reynolds, T.J. (1998) Evolution of an intrusion-
- centered hydrothermal system; Far southeast-Lepanto porphyry and epithermal Cu-Au
- deposits, Philippines. Economic Geology, 93, 373–404.

- Herrington, R., and Wilkinson, J. (1993) Colloidal gold and silica in mesothermal vein
- 717 systems. Geology, 21, 539–542.
- Holwell, D.A., Fiorentini, M., McDonald, I., Lu, Y., Giuliani, A., Smith, D. J., Keith, M.,
- and Locmelis, M. (2019) A metasomatized lithospheric mantle control on the
- metallogenic signature of post-subduction magmatism. Nature Communications, 10,
- 721 3511.
- Jahn, B.M. (2004) The Central Asian Orogenic Belt and growth of the continental crust in
- the Phanerozoic, in Malpas, J., Fletcher, C.J.N., Ali, J.R., and Aitchison, J.C., ed.,
- Aspects of the Tectonic Evolution of China. Geological Society, London, 73–100.
- Jahn, B.M., Wu, F.Y., and Chen, B. (2000) Massive granitoids generation in central Asia:
- Nd isotopic evidence and implication for continental growth in the Phanerozoic.
- 727 Episodes, 23, 82–92.
- Jenkin, G.R.T., Graham, H., Smith, D.J., Khan, R., Abbott, A.P., Harris, R.C., Holwell,
- D.A., Graham, S.D., Khan, R., and Stanley, C.J. (2019) Gold and critical element
- recovery with environmentally benign Deep Eutectic Solvents. 15th SGA Biennial
- 731 Meeting abstract, 4, 1512–1515.
- Jensen, E.P., and Barton, M.D. (2000) Gold deposits related to alkaline magmatism, in
- Hagemann, S.G., and Brown, P.E., eds., Gold in 2000. Society of Economic Geologists,
- 734 Inc., 279–314.

- John, D.A., Hofstra, A.H., Fleck, R.J., Brummer, J.E., and Saderholm, E.C. (2003)
- Geologic setting and genesis of the Mule Canyon low-sulfidation epithermal gold-
- silver deposit, north-central Nevada. Economic Geology, 98, 425–463.
- Keith, M., Smith, D.J., Doyle, K., Holwell, D.A., Jenkin, G.R.T., Barry, T.L., Becker, J.,
- and Rampe, J. (2020) Pyrite chemistry: A new window into Au-Te ore-forming
- processes in alkaline epithermal districts, Cripple Creek, Colorado. Geochimica et
- 741 Cosmochimica Acta, 274, 172–191.
- Kelley, K.D., and Spry, P.G. (2016) Critical elements in alkaline igneous rock-related
- epithermal gold deposits, in Verplanck, P.L., and Hitzman, M.W., eds., Rare Earth and
- Critical Elements in Ore Deposits. Society of Economic Geologists, Inc., 195–216.
- Kelley, K.D., Romberger, S.B., Beaty, D.W., Pontius, J.A., Snee, L.W., Stein, H.J., and
- Thompson, T.B. (1998) Geochemical and geochronological constraints on the genesis
- of Au-Te deposits at Cripple Creek, Colorado. Economic Geology, 93, 981–1012.
- Kelly, J.L., Fu, B., Kita, N.T., and Valley, J.W. (2007) Optically continuous silcrete quartz
- cements of the St. Peter Sandstone: high precision oxygen isotope analysis by ion
- microprobe. Geochimica et Cosmochimica Acta, 71, 3812–3832.
- Kita, N.T., Ushikubo, T., Fu, B., and Valley, J.W. (2009) High precision SIMS oxygen
- isotope analysis and the effect of sample topography. Chemical Geology, 264, 43–57.
- Li, J.Y. (2006) Permian geodynamic setting of Northeast China and adjacent regions:
- closure of the Paleo-Asian Ocean and subduction of the Paleo-Pacific Plate. Journal of
- 755 Asian Earth Sciences, 26, 207–224.

- Li, Z.Z., Qin, K.Z., Li, G.M., Jin, L.Y., Song, G.X., and Han, R. (2019) Incursion of
- meteoric water triggers molybdenite precipitation in porphyry Mo deposits: A case
- study of the Chalukou giant Mo deposit. Ore Geology Reviews, 109, 144–162.
- Liu, J.L., Bai, X.D., Zhao, S.J., Tran, M.D., Zhang, Z.C., Zhao, Z.D., Zhao, H.B., and Lu,
- J. (2011) Geology of the Sandaowanzi telluride gold deposit of the northern Great
- Xing'an Range, NE China: Geochronology and tectonic controls. Journal of Asian
- 762 Earth Sciences, 41, 107–118.
- 763 Liu, J.L., Zhao, S.J., Cook, N.J., Bai, X.D., Zhang, Z.C., Zhao, Z.D. and Lu, J. (2013)
- Bonanza-grade accumulations of gold tellurides in the Early Cretaceous Sandaowanzi
- deposit, northeast China. Ore Geology Reviews, 54, 110–126.
- Miao, L.C., Fan, W.M., Zhang, F.Q., Liu, D.Y., Jian, P., Shi, G.H., Tao, H., and Shi, Y.R.
- 767 (2004) Zircon SHRIMP geochronology of the Xinkailing-Kele complex in the
- northwestern Lesser Xing'an Range, and its geological implications. Chinese Science
- 769 Bulletin, 49, 201–209.
- 770 Miao, L.C., Liu, D.Y., Zhang, F.Q., Fan, W.M., Shi, Y.R., and Xie, H.Q. (2007) Zircon
- SHRIMP U-Pb ages of the "Xinghuadukou Group" in Hanjiayuanzi and Xinlin areas
- and the "Zhalantun Group" in Inner Mongolia, Da Hinggan Mountains. Chinese
- 773 Science Bulletin, 52, 1112–1124.
- Miao, L.C., Zhang, F.O., Zhu, M.S., and Liu, D.Y. (2015) Zircon SHRIMP U-Pb dating of
- metamorphic complexes in the conjunction of the Greater and Lesser Xing'an ranges,

- NE China: Timing of formation and metamorphism and tectonic implications. Journal
- of Asian Earth Sciences, 114, 634–648.
- Moncada, D., Mutchler, S., Nieto, A., Reynolds, T.J., Rimstidt, J.D., and Bodnar, R.J. (2012)
- Mineral textures and fluid inclusion petrography of the epithermal Ag-Au deposits at
- Guanajuato, Mexico: Application to exploration. Journal of Geochemical Exploration,
- 781 114, 20–35.
- O'Neil, J.R., and Silberman, M.L. (1974) Stable isotope relations in epithermal Au-Ag
- deposits. Economic Geology, 69, 902–909.
- O'Neil, J.R., and Taylor, H.P., Jr. (1967) The oxygen isotope and cation exchange
- chemistry of feldspars. American Mineralogist, 52, 1414–1437.
- Oster J. L., Kitajima K., Valley J. W., Rogers B. and Maher K. (2017) An evaluation of
- paired δ^{18} O and $(^{234}\text{U}/^{238}\text{U})_0$ in opal as a tool for paleoclimate reconstruction in semi-
- arid environments. Chemical Geology, 449, 236–252.
- 789 Pei, F.P., Xu, W.L., Yang, D.B., Zhao, Q.G., Liu, X.M., and Hu, Z.C. (2007) Zircon U-Pb
- 790 geochronology of basement metamorphic rocks in the Songliao Basin. Chinese
- 791 Science Bulletin, 52, 942–948.
- Peres, P., Kita, N.T., Valley, J.W., Fernandes, F., and Schuhmacher, M. (2013) New
- sample holder geometry for high precision isotope analyses: Surface and Interface
- 794 Analysis, 45, 553–556.
- 795 Pollington A.D. (2013) Stable isotope signatures of diagenesis. natural and experimental
- studies. Ph.D. thesis, University of Wisconsin, Madison.

- Prokofiev, V.Y., Kamenetsky, V.S., Selektor, S.L., Rodemann, T., Kovalenker, V.A., and
- Vatsadze, S.Z. (2016) First direct evidence for natural occurrence of colloidal silica in
- chalcedony-hosted vacuoles and implications for ore-forming processes. Geology, 45,
- 800 71–74.
- 801 Qu, G.S. (2008) Lithostratigraphy of Heilongjiang province, China. China University of
- Geosciences Press, Wuhan, China, 1–301 (in Chinese).
- 803 Reed, M.H. (1982) Calculation of multicomponent chemical equilibria and reaction
- processes in systems involving minerals gases and an aqueous phase. Geochimica et
- 805 Cosmochimica Acta, 46, 513–528.
- Reed, M.H. (1998) Calculation of simultaneous chemical equilibria in aqueous-mineral-
- gas systems and its application to modeling hydrothermal processes, in Richards, J.P.,
- and Larson, P.B., ed., Techniques in Hydrothermal Ore Deposits Geology. Society of
- Economic Geologists, Inc., 10, 109–124.
- 810 Reed, M.H. and Spycher, N.F. (1985) Boiling, cooling, and oxidation in epithermal
- systems: A numerical modeling approach, in Berger, B.R., and Bethke, P.M., ed.,
- Geology and Geochemistry of Epithermal Systems. Society of Economic Geologists,
- 813 Inc., 249–272.
- 814 Saunders, J.A. (1990) Colloidal transport of gold and silica in epithermal precious-metal
- systems: Evidence from the Sleeper deposit, Nevada. Geology, 18, 757–760.

- Saunders, J.A. (1994) Silica and gold textures in bonanza ores of the Sleeper Deposit,
- Humboldt County, Nevada; evidence for colloids and implications for epithermal ore-
- forming processes. Economic Geology, 89, 628–638.
- 819 Saunders, J.A., and Brueseke, M.E. (2012) Volatility of Se and Te during subduction-
- related distillation and the geochemistry of epithermal ores of the western United
- 821 States. Economic Geology, 107, 165–172.
- 822 Saunders, J.A., and Schoenly, P.A. (1995) Boiling, colloid nucleation and aggregation, and
- the genesis of bonanza Au-Ag ores of the Sleeper deposit, Nevada. Mineralium
- 824 Deposita, 30, 199–210.
- Saunders, J.A., Unger, D.L., Kamenov, G.D., Fayek, M., Hames, W.E., and Utterback, W.C.
- 826 (2008) Genesis of Middle Miocene Yellowstone hotspot-related bonanza epithermal
- 827 Au–Ag deposits, Northern Great Basin, USA. Mineralium Deposita, 43, 715–734.
- 828 Sengör, A.M.C., Natal'in, B.A., and Burtman, V.S. (1993) Evolution of the Altaid tectonic
- collage and Paleozoic crustal growth in Eurasia. Nature, 364, 299–307.
- 830 Shelton, K.L., So, C.S., Haeussler, G.T., Chi, S.J., and Lee, K.Y. (1990) Geochemical
- studies of the Tongyoung gold-silver deposits, Republic of Korea; evidence of
- meteoric water dominance in a Te-bearing epithermal system. Economic Geology, 85,
- 833 1114–1132.
- 834 Shimizu, T. (2014) Reinterpretation of quartz textures in terms of hydrothermal fluid
- evolution at the Koryu Au-Ag deposit, Japan. Economic Geology, 109, 2051–2065.

- 836 Shimizu, T., Matsueda, H., Ishiyama, D., and Matsubaya, O. (1998) Genesis of epithermal
- Au-Ag mineralization of the Koryu mine, Hokkaido, Japan. Economic Geology, 93,
- 838 303–325.
- Simmons, S.F. (1995) Magmatic contributions to low-sulfidation epithermal deposits, in
- Magmas, fluids and ore deposits. Mineralogical Association of Canada Short Course
- 841 Series, 23, 455–477.
- Simmons, S.F., and Browne, P.R.L. (2000) Hydrothermal minerals and precious metals in
- the Broadlands-Ohaaki geothermal system: Implications for understanding low-
- sulfidation epithermal deposits. Economic Geology, 95, 971–1000.
- Simmons, S.F., and Christenson, B.W. (1994) Origins of calcite in a boiling geothermal
- system. American Journal of Science, 294, 361–400.
- Simmons, S.F., Brown, K.L., and Tutolo, B.M. (2016) Hydrothermal Transport of Ag, Au,
- 848 Cu, Pb, Te, Zn, and Other Metals and Metalloids in New Zealand Geothermal Systems:
- Spatial Patterns, Fluid-Mineral Equilibria, and Implications for Epithermal
- Mineralization. Economic Geology, 111, 589–618.
- 851 Simmons, S.F., White, N.C., and John, D.A. (2005) Geological characteristics of
- epithermal precious and base metal deposits, in Hedenquist, J.W., Thompson, J.F.H.,
- Goldfarb, R.J., and Richards, J.P., ed., One Hundredth Anniversary Volume, Society
- of Economic Geologists, Inc., 485–522.

- Simpson, M.P., and Mauk, J.L. (2011) Hydrothermal alteration and veins at the epithermal
- Au-Ag deposits and prospects of the Waitekauri Area, Hauraki Goldfield, New
- Zealand. Economic Geology, 106, 945–973.
- 858 Simpson, M.P., Palinkas, S.S., Mauk, J.L., and Bodnar, R.J. (2015) Fluid inclusion
- chemistry of adularia-sericite epithermal Au-Ag deposits of the southern Hauraki
- Goldfield, New Zealand. Economic Geology, 110, 763–786.
- 861 Smith, M.P., Savary, V., Yardley, B.W.D., Valley, J.W. Royer, J.J., and Dubois, M. (1998)
- The evolution of the deep flow regime at Soultz-sous-Forfts, Rhine Graben, eastern
- France: Evidence from a composite quartz vein. Journal of Geophysical Research, 103,
- 864 27,223–27,237
- Spry, P.G., Chryssoulis, S., and Ryan, C.G. (2004) Process mineralogy of gold: Gold from
- telluride-bearing ores. JOM, 56, 60–62.
- 867 Spry, P.G., Paredes, M.M., Foster, F., Truckle, J.S., and Chadwick, T.H. (1996) Evidence
- for a genetic link between gold-silver telluride and porphyry molybdenum
- mineralization at the Golden Sunlight Deposit, Whitehall, Montana; fluid inclusion
- and stable isotope studies. Economic Geology, 91, 507–526.
- 871 Sui, Z.M., Ge, W.C., Wu, F.Y., Zhang, J.H., Xu, X.C., and Cheng, R.Y. (2007) Zircon U-
- Pb ages geochemistry and its petrogenesis of Jurassic granites in northeastern part of
- the Da Hinggan Mts. Acta Petrologica Sinica, 23, 461–480 (in Chinese with English
- abstract).

- 875 Steele-MacInnis, M., Lecumberri-Sanchez, P., and Bodnar, R.J. (2012)
- HOKIEFLINCS_H₂O-NACL: A Microsoft Excel spreadsheet for interpreting
- microthermometric data from fluid inclusions based on the PVTX properties of H₂O-
- NaCl. Computers & Geosciences, 49, 334–337.
- 879 Taksavasu, T., Monecke, T., and Reynolds, T. (2018) Textural characteristics of
- 880 noncrystalline silica in sinters and quartz veins: Implications for the formation of
- bonanza veins in low-sulfidation epithermal deposits. Minerals, 8, 331.
- Tanner, D., Henley, R.W., Mavrogenes, J.A., and Holden, P. (2013) Combining in situ
- isotopic trace element and textural analyses of quartz from four magmatic-
- hydrothermal ore deposits. Contributions to Mineralogy and Petrology, 166, 1119–
- 885 1142.
- Taylor, H.P. (1997) Oxygen and hydrogen isotope relationships in hydrothermal mineral
- deposits, in Barnes, H.L., ed., Geochemistry of Hydrothermal Ore Deposits. New York,
- Wiley–Interscience, 229–302.
- Valley, J.W., and Graham, C.M. (1996) Ion microprobe analysis of oxygen isotope ratios
- in quartz from Skye granite: healed micro-cracks, fluid flow, and hydrothermal
- exchange. Contributions to Mineralogy and Petrology, 124, 225–234.
- Valley, J.W., and Kita, N.T. (2009) In situ oxygen isotope geochemistry by ion microprobe,
- in Fayek, M., ed., Secondary Ion Mass Spectrometry in the Earth Sciences: Gleaning
- the big picture from a small spot. Mineralogical Association of Canada, Short Course,
- 895 41, 19–63.

- Valley, J.W., Graham, C.M., Harte, B., Kinny, P., and Eiler, J.M. (1998) Ion microprobe
- analysis of oxygen, carbon, and hydrogen isotope ratios, in McKibben, M.A., Shanks,
- 898 III, W.C. and Ridley W.I., ed., Applications of Microanalytical Techniques to
- Understanding Mineralizing Processes: Society of Economic Geologists, Inc., 7, 73–
- 900 98.
- Voudouris, P. (2006) A comparative mineralogical study of Te-rich magmatic-hydrothermal
- systems in northeastern Greece. Mineralogy and Petrology, 87, 241–275.
- 903 Wang, P.J., Liu, Z.J., Wang, S.X., and Song, W.H. (2002) 40Ar/39Ar and K/Ar dating of the
- volcanic rocks in the Songliao basin, NE China: constraints on stratigraphy and basin
- dynamics. International Journal of Earth Sciences, 91, 331–340.
- Wang, X.L., Coble, M.A., Valley, J.W., Shu, X.J., Kitajima, K., Spicuzza, M.J., and Sun,
- T. (2014) Influence of radiation damage on Late Jurassic zircon from southern China.
- evidence from in situ measurements of oxygen isotopes, laser Raman, U-Pb ages, and
- trace elements. Chemical Geology, 389, 122–136.
- Wang, Y., Zhang, F.Q., Zhang, D.W., Miao, L.C., Li, T.S., Xie, H.Q., Meng, Q.R., and Liu,
- D.Y. (2006) Zircon SHRIMP U-Pb dating of meta-diorite from the basement of the
- 912 Songliao Basin and its geological significance. Chinese Science Bulletin, 51, 1877–
- 913 1883.
- 914 Wedepohl, K.H. (1995) The composition of the continental crust. Geochimica et
- 915 Cosmochimica Acta, 59, 1217–1232.
- 916 Williams-Jones, A.E., and Heinrich, C.A. (2005) Vapor transport of metals and the

- formation of magmatic-hydrothermal ore deposits, in Hedenquist, J.W., Thompson,
- J.F.H., Goldfarb, R.J., and Richards, J.P., ed., One Hundredth Anniversary Volume,
- 919 Society of Economic Geologists, Inc., 1287–1312.
- 920 Wu, F.Y., Lin, J.Q., Wilde, S.A., Zhang, X.O., and Yang, J.H. (2005b) Nature and
- significance of the Early Cretaceous giant igneous event in eastern China. Earth and
- Planetary Science Letters, 233, 103–119.
- 923 Wu, F.Y., Sun, D.Y., Li, H.M., and Wang, X.L. (2000) Zircon U-Pb ages of the basement
- rocks beneath the Songliao Basin, NE China. Chinese Science Bulletin, 45, 1514–1518.
- Wu, F.Y., Sun, D.Y., Li, H.M., and Wang, X.L. (2001) The nature of basement beneath the
- Songliao Basin in NE China. geochemical and isotopic constraints: Physics and
- 927 Chemistry of the Earth. Part A. Solid Earth and Geodesy, 26, 793–803.
- 928 Wu, F.Y., Yang, J.H., Lo, C.H., Wilde, S.A., Sun, D.Y., and Jahn, B.M. (2007) The
- Heilongjiang Group: a Jurassic accretionary complex in the Jiamusi Massif at the
- western Pacific margin of northeastern China. Island Arc, 16, 156–172.
- 931 Wu, Z., Wang, H., Xu, D., and Zhou, Y. (2005a) Geology and geochemistry of the
- 932 Sandaowanzi gold deposit, Heilongjiang province, NE China. Geological Review, 51,
- 933 264–267 (in Chinses with English abstract).
- 934 Xu, H., Yu, Y.X., Wu, X.K., Yang, L.J., Tian, Z., Gao, S., and Wang, Q.S. (2012)
- Intergrowth texture in Au-Ag-Te minerals from Sandaowanzi gold deposit
- Heilongjiang Province: Implications for ore-forming environment. Chinese Science
- 937 Bulletin, 57, 2778–2786.

- Yang, T. (2008) Volcanic rocks and their relationships to the gold mineralization in the
- Dong'an deposit, NE China. M.Sc. thesis, Beijing, China, China University of
- Geosciences (Beijing), 70–72 (in Chinese with English abstract).
- 941 Yu, Y.X., Xu, H., Wu, X.K., Yang, L.J., Tian, Z., Gao, S., and Wang, Q.S. (2012)
- Characteristics of the Au-Ag-Te minerals and its ore-forming fluids in Sandaowanzi
- gold deposit Heilongjiang Province. Acta Petrologica Sinica, 28, 345–356 (in Chinese
- with English abstract).
- 245 Zhai, D., and Liu, J. (2014) Gold-telluride-sulfide association in the Sandaowanzi
- epithermal Au-Ag-Te deposit, NE China: implications for phase equilibrium and
- physicochemical conditions. Mineralogy and Petrology, 108, 853–871.
- 248 Zhai, D., Williams-Jones, A.E., Liu, J., Tombros, S.F., and Cook, N.J. (2018) Mineralogical
- 949 fluid inclusion and multiple isotope (H-O-S-Pb) constraints on the genesis of the
- 950 Sandaowanzi epithermal Au-Ag-Te deposit, NE China. Economic Geology, 113,
- 951 1359–1382.
- 952 Zhang, J.H., Gao, S., Ge, W.C., Wu, F.Y., Yang, J.H., Wilde, S.A., and Li, M. (2010b)
- Geochronology of the Mesozoic volcanic rocks in the Great Xing'an Range
- northeastern China: Implications for subduction-induced delamination. Chemical
- 955 Geology, 276, 144–165.
- 256 Zhang, J.H., Ge, W.C., Wu, F.Y., Wilde, S.A., Yang, J.H., and Liu, X.M. (2008) Large-scale
- Early Cretaceous volcanic events in the northern Great Xing'an Range, northeastern
- 958 China. Lithos, 102, 138–157.

959	Zhang, Z., Mao, J., Wang, Y., Pirajno, F., Liu, J., and Zhao, Z. (2010a) Geochemistry and
960	geochronology of the volcanic rocks associated with the Dong'an adularia-sericite
961	epithermal gold deposit, Lesser Hinggan Range, Heilongjiang province, NE China:
962	Constraints on the metallogenesis. Ore Geology Reviews, 37, 158–174.
963	Zhao, Z.H., Sun, J.G., Li, G.H., Xu, W.X., Lü, C.L., Wu, S., Guo, Y., Liu, J., and Ren, L.
964	(2019) Early Cretaceous gold mineralization in the Lesser Xing'an Range of NE China
965	the Yongxin example. International Geology Review, 61, 1522–1549.
966	Zhou, L., Guo, J., Liu, B., and Li, L. (2001) Structural state of adularia from Hishikari,
967	Japan. Chinese Science Bulletin, 46, 950–953.
968	
969	
970	List of figure captions
971	

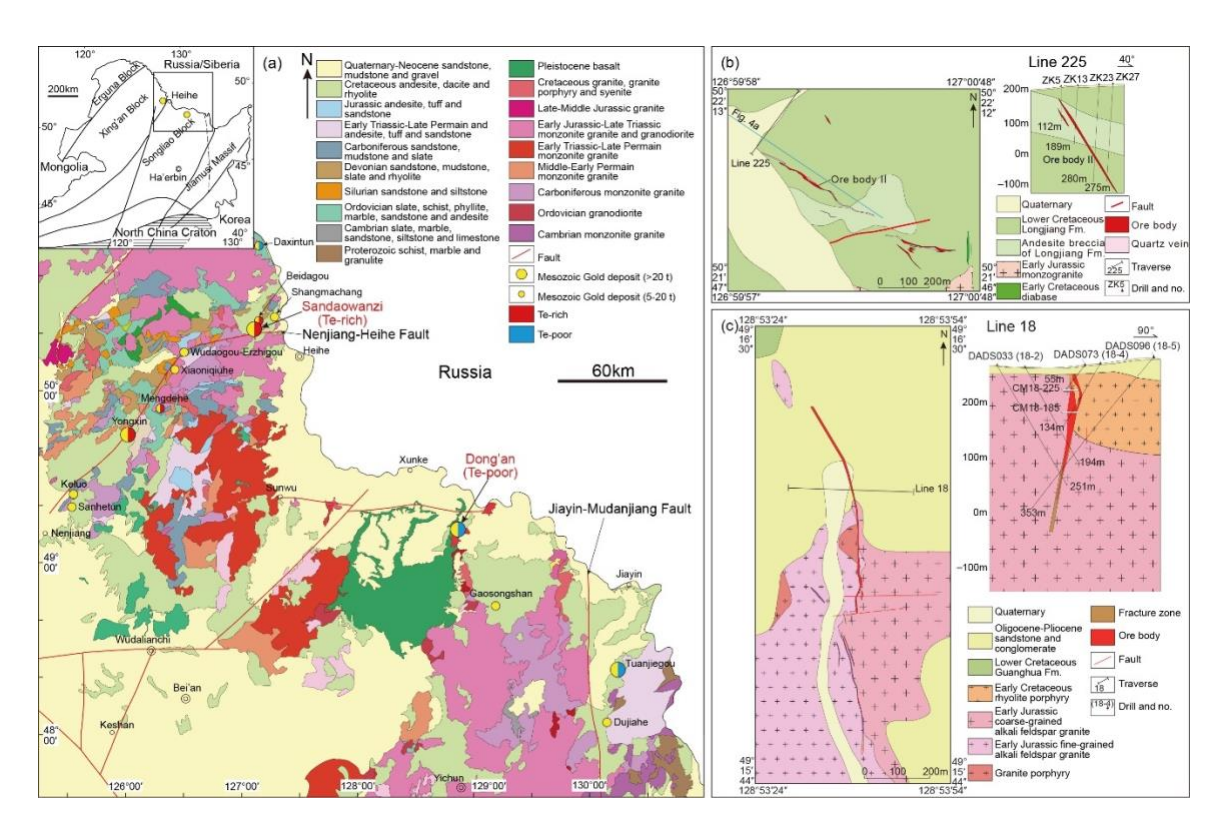


Fig. 1. (a) Regional geologic map showing the location of Au-Ag deposits in north Heilongjiang province, NE China (after Gao 2017; Zhao et al. 2019). The inset shows the location of the regional map relative to crustal blocks in NE China. Geologic map and cross section of Sandaowanzi (b) (after Liu et al. 2013; Gao et al. 2017) and Dong'an (c) (after Zhang et al. 2010a).

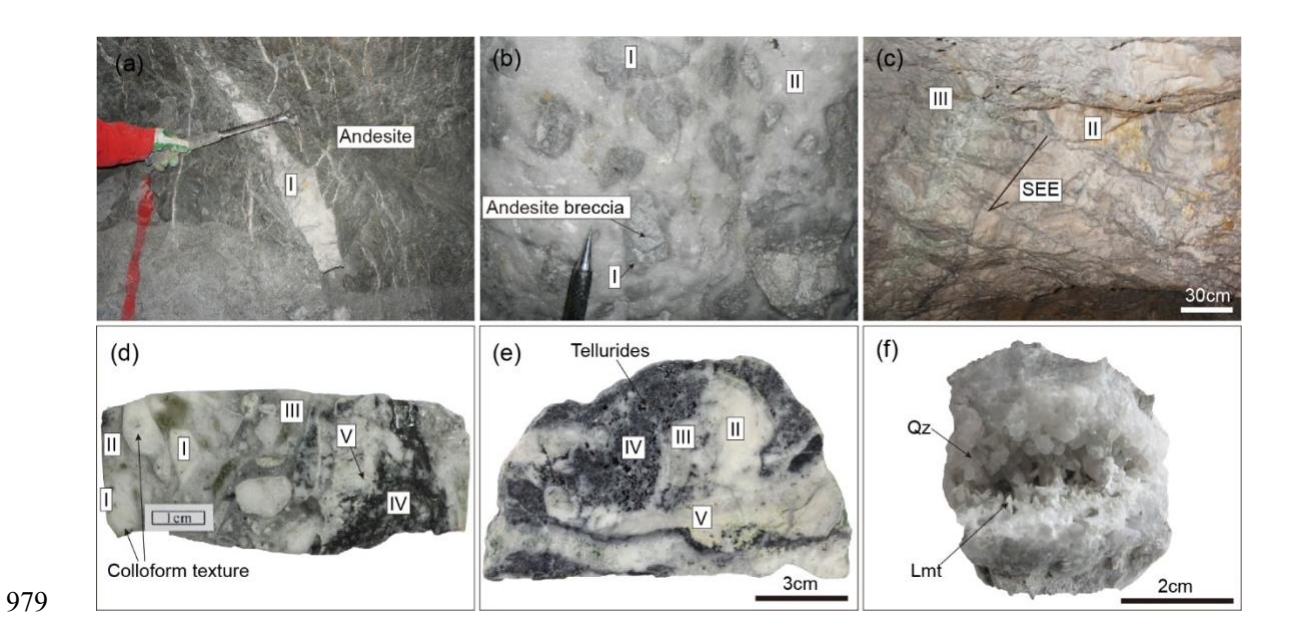


Fig. 2. Photos of multiple generations of quartz from Sandaowanzi. (a). Photo of Stage I quartz veins hosted by andesite from underground. (b). Photo of brecciated Stage I vein quartz cemented by the Stage II quartz from underground. (c). Photo of Stage II and Stage III quartz veins from underground. (d-e). Photos of five stages of quartz and tellurides in the ore. (f). Photo of early quartz vug with late euhedral laumontite. Roman numeral is

Abbreviations: Adl=Adularia. Chc=Chalcedony. Lmt=Laumontite. Qz=Quartz.

quartz stage.

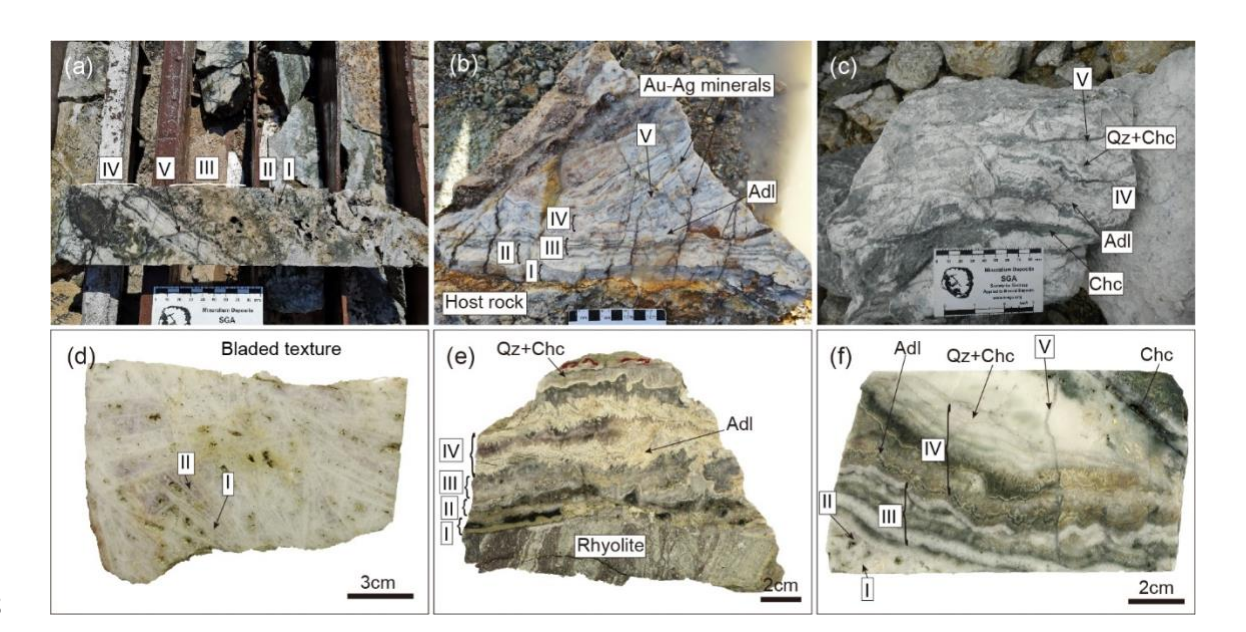


Fig. 3. Photos of multiple generations of quartz from Dong'an. (a). Photo of five generations of quartz with early bladed and late colloform textures in drill core. Early bladed textures cross-cut by late colloform textures. (b) Photo of ore-bearing colloform textures from open pit. Stage I, II, II, IV quartz in vein hosted by altered rhyolite, and cross-cut by Stage 5 thin quartz veinlets. (c) Photo of Stage IV quartz, chalcedony and adularia cross-cut by Stage V thin quartz veinlets from open pit. (d). Photo of early bladed quartz textures that are barren of gold. (e). Photo of colloform texture vein with four stages of quartz hosted in altered rhyolite. (f). Photo of ore-bearing colloform vein. As in b, four stages of quartz are cut by Stage V thin quartz veinlets. Roman numeral is quartz stage.

Abbreviations: Adl=Adularia. Chc=Chalcedony. Lmt=Laumontite. Qz=Quartz

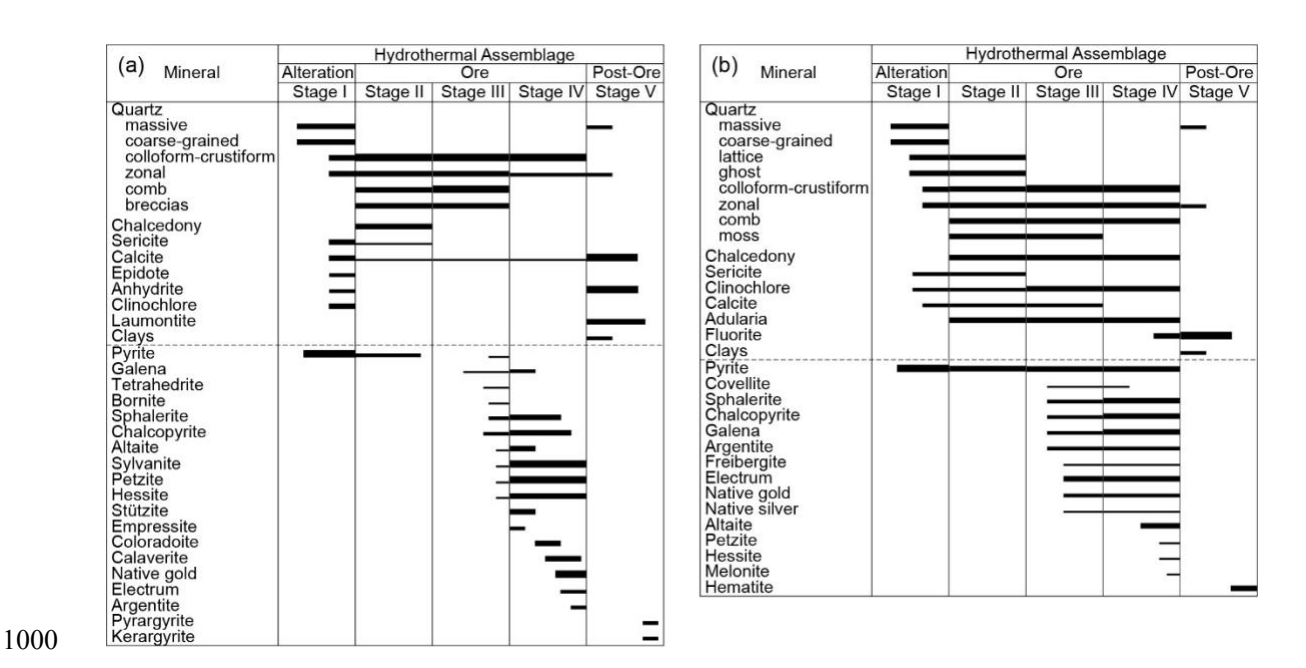


Fig. 4. Paragenesis of ore and gangue minerals in the veins. (a). Sandaowanzi deposit. (b). Dong'an deposit.

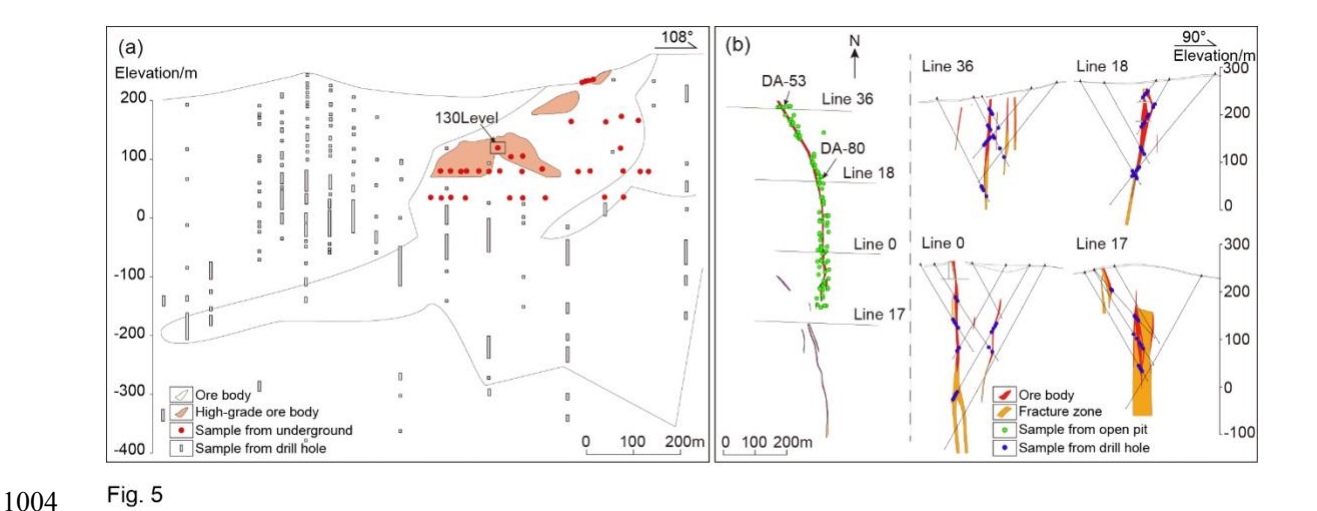


Fig. 5. Sample locations from underground, open pit and drill holes. (a). Longitudinal vertical projection of Sandaowanzi veins. (b). Plane map and cross section of Dong'an veins.

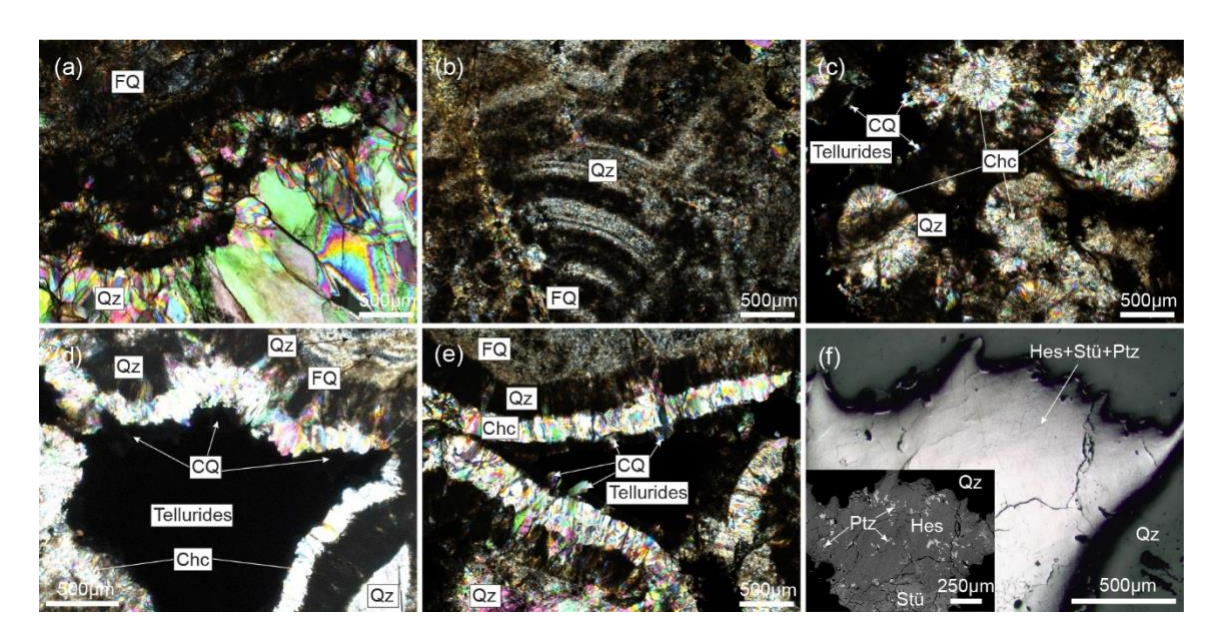
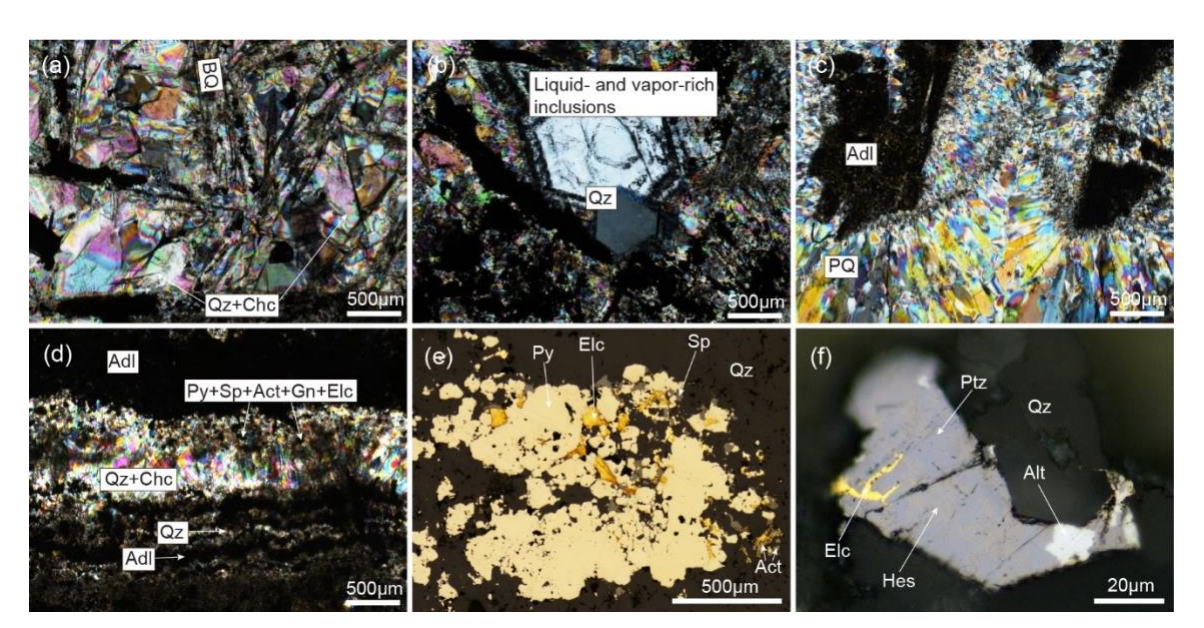


Fig. 6. Representative photos of quartz textures under crossed polars in transmitted light (a-e, sample thickness ~200 μm), and ore minerals in reflected light (f) from Sandaowanzi. (a). Colloform texture consisting of fine-grained quartz with a jigsaw texture and crystalline quartz with granoblastic texture. (b). Thin colloform texture with alternating bands of fine-grained jigsaw texture quartz and crystalline quartz. (c-e). Chalcedony, dark quartz and crystalline quartz with a comb texture followed by tellurides. (j). Coarse-grained hessite, stützite and petzite associated with comb quartz from figure d.

Abbreviations: Chc=Chalcedony. Qz=Quartz. Hes=Hessite. Ptz=Petzite. Stü=Stützite. CQ=Comb quartz. FQ=Fine-grained quartz.



1021

1022

1023

1024

1025

1026

1027

1028

1029

1030

Fig. 7. Representative photos of quartz textures under crossed polars in transmitted light (a-d, sample thickness ~200 μm), and ore minerals in reflected light (e-f) from Dong'an. (a). Bladed quartz followed by chalcedonic quartz. (b) Quartz crystals with liquid- and vapor-rich inclusions in flamboyant texture. (c). Dark adularia crystals followed by plumose quartz. (d). Adularia and quartz bands with sulfides, tellurides and electrum. (e). Pyrite, sphalerite, argentite and electrum in colloform bands from figure d. (f). Rare finegrained hessite, petzite, altaite and electrum. Abbreviations: Act=Acanthite. Adl=Adularia. Alt=Altaite. Chc=Chalcedony. Elc=Electrum. Gn=Galena. Hes=Hessite. Ptz=Petzite. Py=Pyrite. Qz=Quartz. Sp=Sphalerite. BQ=Bladed quartz. PQ=Plumose quartz.

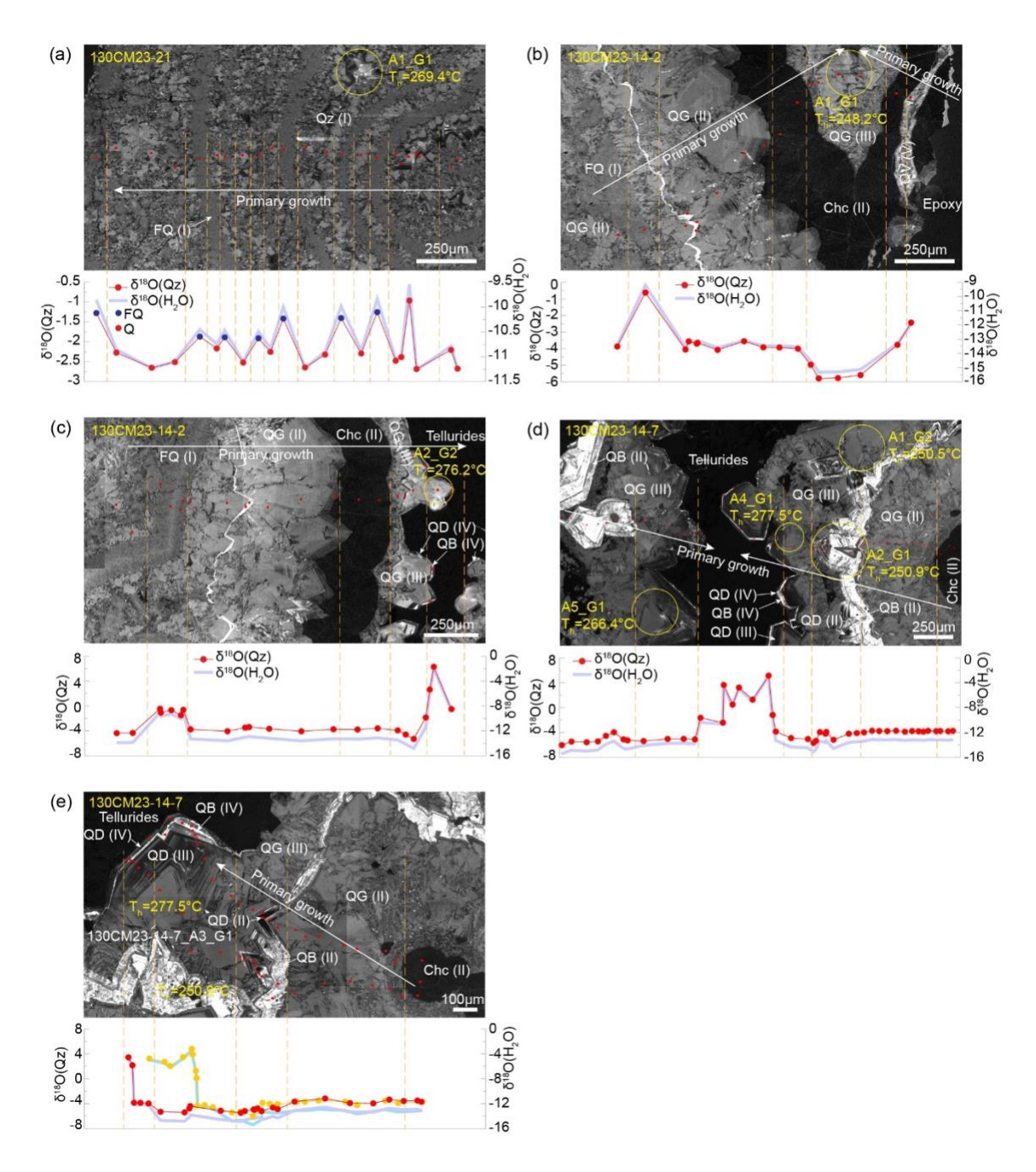


Fig. 8. CL images of quartz and chalcedony from Sandaowanzi. SIMS oxygen isotope spots are in red, and homogenization temperatures of fluid inclusion assemblages are outlined in yellow. The orange dashed lines show how each band of quartz correlates with the oxygen isotope profile in red and corresponding fluid composition in blue. The quartz-water fractionation factor from Clayton et al. (1972) and Friedman and O'Neil (1977) and fluid

inclusion homogenization temperature from each band were used to calculate δ¹⁸O(H₂O).
In bands where fluid inclusions are absent, temperature data from adjacent bands were used.
(a). Colloform quartz with thin layer. (b and c). Fine grained, drusy, and chalcedonic quartz
without tellurides (b) and with abundant tellurides (c). (d and e). Chalcedonic, fine-grained,
and crystal quartz with abundant tellurides.
Abbreviations: Chc=Chalcedony. Qz=Quartz. FQ=Fine-grained quartz. QB=Quartz with
CL-bright. QD=Quartz with CL-dark. QG=Quartz with CL-gray. QV=Quartz vein (Thin).

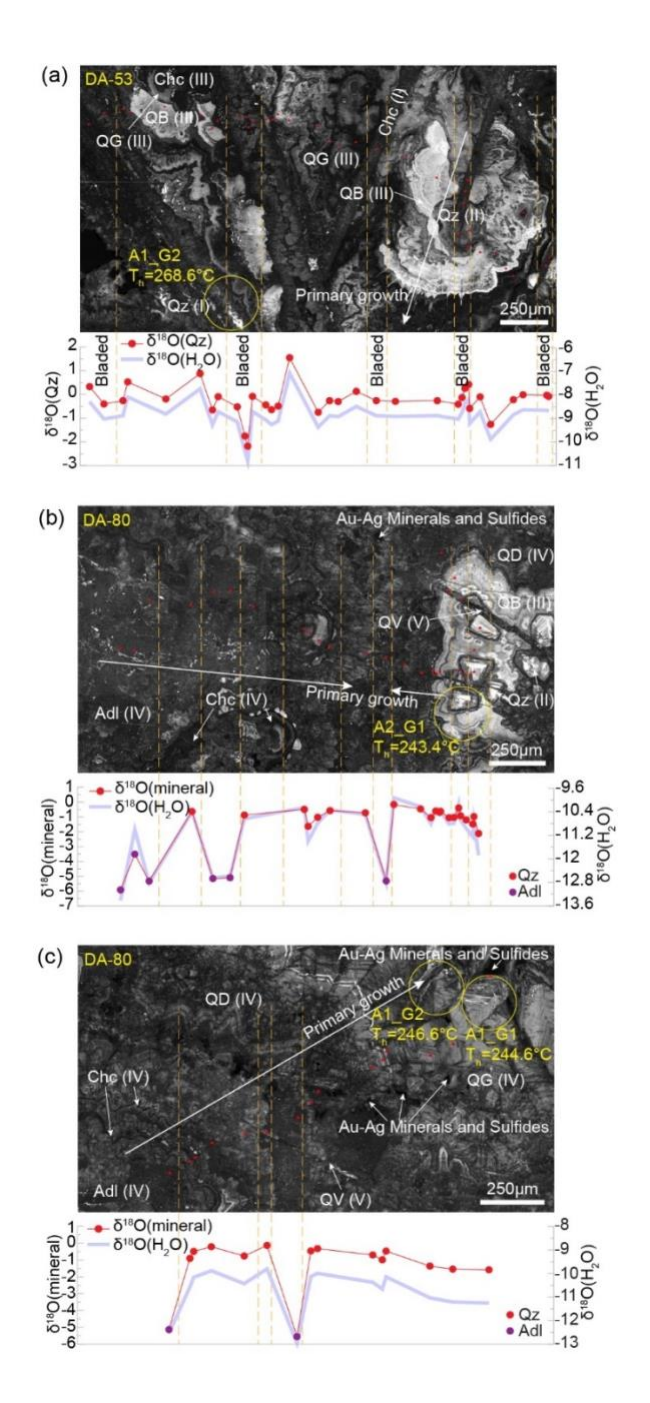


Fig. 9. CL images of quartz, chalcedony and adularia at Dong'an. SIMS oxygen isotope spots are in red, and homogenization temperatures of fluid inclusion assemblages are outlined in yellow. The orange dashed lines show how each band of quartz correlates with the oxygen isotope profile in red and corresponding fluid composition in blue. The quartz-water fractionation factor from Clayton et al. (1972) and Friedman and O'Neil (1977) and

fluid inclusion homogenization temperature from each band were used to calculate $\delta^{18}O(H_2O)$. The K-feldspar-water fractionation factor from O'Neil and Taylor (1967) fluid inclusion homogenization temperature from quartz in the same band with adularia were used to calculate $\delta^{18}O(H_2O)$. In bands where fluid inclusions are absent, temperature data from adjacent bands were used. (a). Barren ghost-bladed texture quartz. (b and c). Colloform and cockade texture (b) and colloform texture (c) with minor Au-Ag minerals. Abbreviations: Adl=Adularia. Chc=Chalcedony. Qz=Quartz. QB=Quartz with CL-bright. QD=Quartz with CL-dark. QG=Quartz with CL-gray. QV=Quartz vein (Thin).



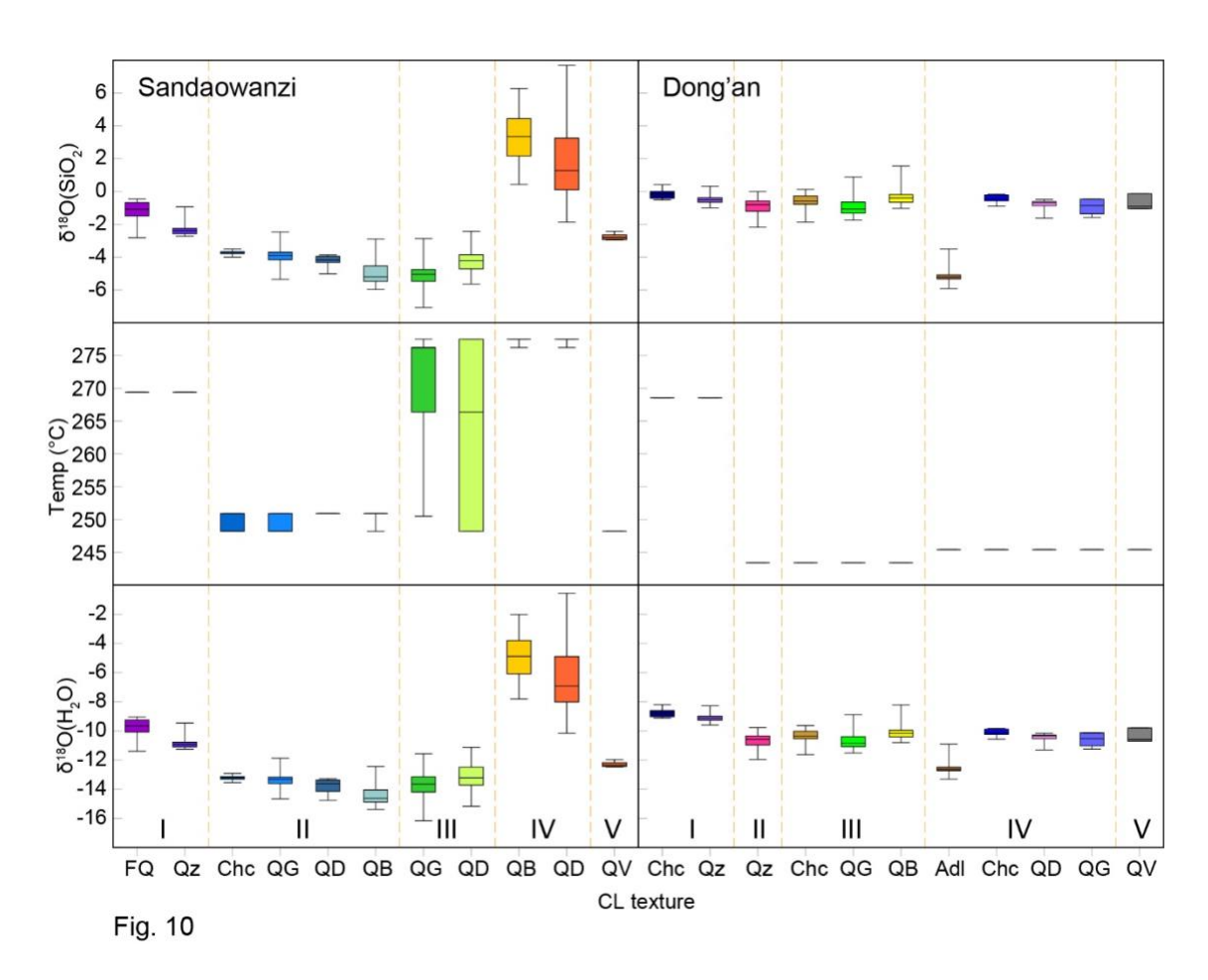


Fig. 10. Box and whisker plots of SIMS $\delta^{18}\text{O}$ data from chalcedony, quartz, and adularia

in the Sandaowanzi and Dong'an deposits. (a and b). Measured δ¹⁸O data. (c and d). Homogenization temperature of fluid inclusions spatially correlated to measured δ¹⁸O data from each band. (e and f). Calculated δ¹⁸O(H₂O) for every SIMS spot. (a, c, and e). Sandaowanzi. (b, d, and f). Dong'an. The orange dashed lines separate each stage. Abbreviations: FQ=Fine-grained quartz. Adl=Adularia. Chc=Chalcedony. Qz=Quartz. QB=Quartz with CL-bright. QD=Quartz with CL-dark. QG=Quartz with CL-gray. QV=Quartz vein (Thin).



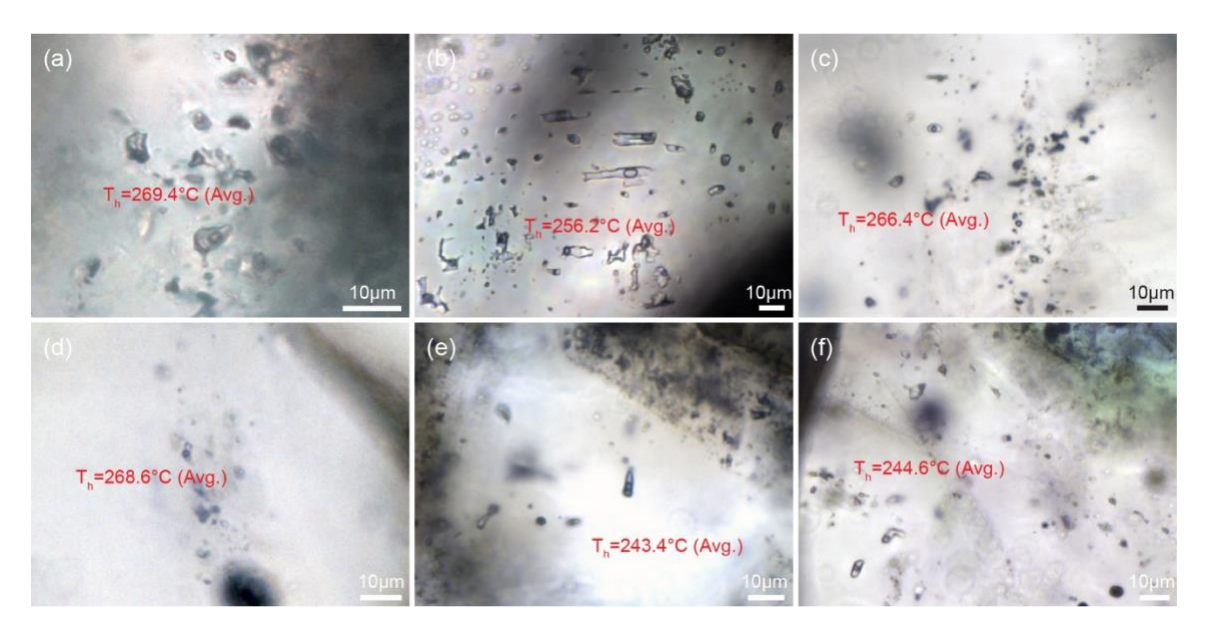


Fig. 11. Images of fluid inclusion assemblages with their average (Avg.) homogenization temperatures (Th) from Sandaowanzi (a-c) and Dong'an (d-f). (a). Fluid inclusion assemblages from thin colloform texture shown on Figure 8a. (b). Fluid inclusion assemblages from CL-bright quartz shown on Figure 8d. (c). Fluid inclusion assemblages from CL-dark quartz near tellurides shown on Figure 8d and e. (d). Fluid inclusion assemblages from ghost-bladed texture shown on Figure 9a. (e). Fluid inclusion

assemblages form CL-bright quartz breccia shown on Figure 9b. (f). Fluid inclusion assemblages form CL-gray quartz near electrum shown on Figure 9c.

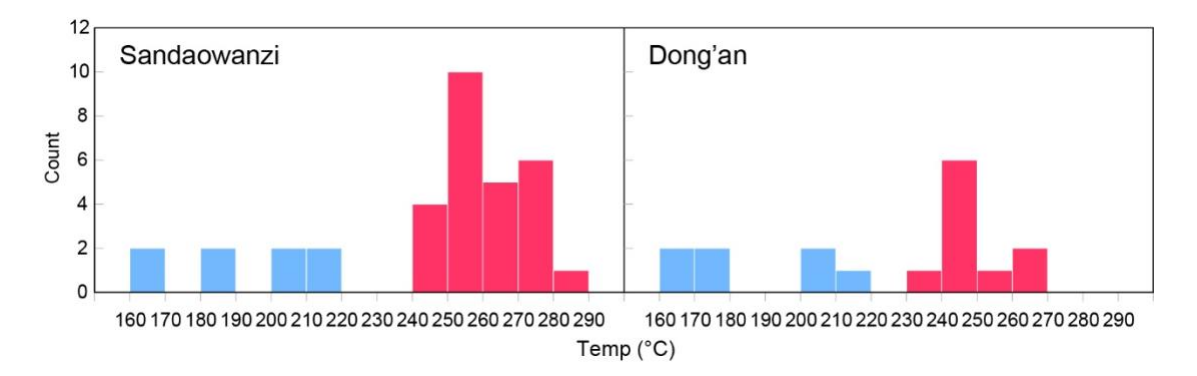


Fig. 12. Histograms of fluid inclusion homogenization temperatures from Sandaowanzi and Dong'an. Red color is primary fluid inclusions, blue color is secondary fluid inclusions.

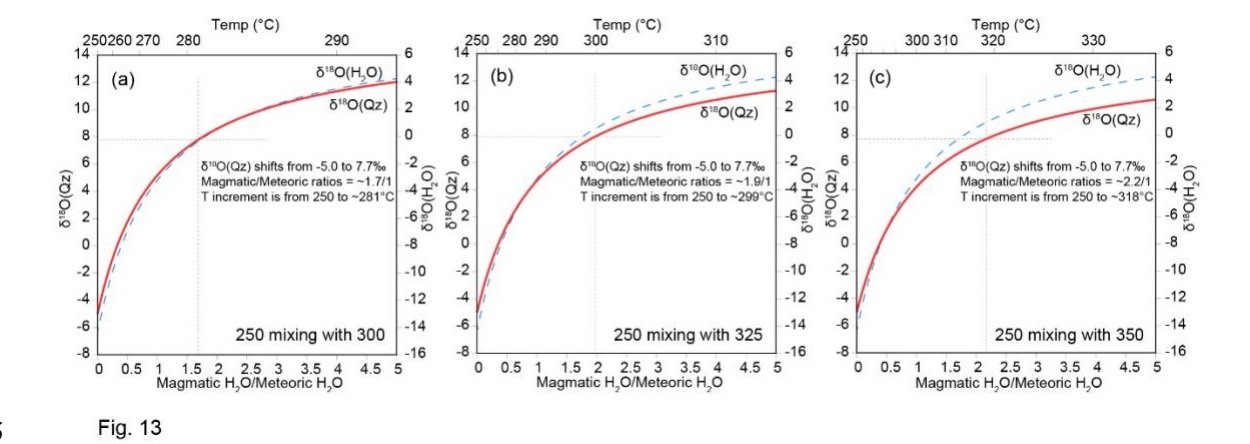


Fig. 13. Diagrams showing the calculated fluid temperature and oxygen isotopic composition of water and quartz as a function of the mixing ratio of magmatic and meteoric water. Meteoric water has an initial temperature of 250 (based on stage III quartz fluid inclusion measurements at Sandaowanzi), and magmatic water has an initial temperature of 300 (a), 325 (b), and 350 (c), respectively. Oxygen isotope values are 8% for magmatic

water (Taylor 1997), and -14.7‰ for meteoric water (after stage III quartz at Sandaowanzi). The temperature of the mixed fluids is based on the enthalpy of water and the mixing increment. The effects of salinity on the enthalpy of water can generally be ignored because they are small (Reed 1998). Because the total mass of precipitated minerals is small in most cases, their heat contributions can be neglected (Reed 1998). The quartz-water fractionation factor used is from Clayton et al. (1972) as corrected by Friedman and O'Neil (1977).

1099 List of tables

1101 Table 1. Bulk oxygen isotope compositions at Sandaowanzi and Dong'an.

Table 2. Compilation of the sample material, mineralogy and applied analytical techniques.

Table 3. Microthermometric data on fluid inclusions from Sandaowanzi and Dong'an.

1107 Appendix A

Table A1. SIMS oxygen isotope data on quartz, chalcedony and adularia from Sandaowanzi and Dong'an.